Ab initio theory of moiré superlattice bands in layered two-dimensional materials

Jeil Jung
The University of Texas at Austin, Austin, Texas 78712, USA and National University of Singapore, 117551 Singapore

Arnaud Raoux
CNRS UMR 8502, Univ. Paris-Sud, F-91405 Orsay, France

Zhenhua Qiao
The University of Texas at Austin, Austin, Texas 78712, USA and University of Science and Technology of China, Hefei, Anhui 230026, China

A. H. MacDonald
The University of Texas at Austin, Austin, Texas 78712, USA

(Received 5 August 2013; revised manuscript received 9 April 2014; published 12 May 2014)

When atomically thin two-dimensional (2D) materials are layered, they often form incommensurate noncrystalline structures that exhibit long-period moiré patterns when examined by scanning probes. In this paper, we present an approach that uses information obtained from *ab initio* calculations performed on short-period crystalline structures to derive effective Hamiltonians that are able to efficiently describe the influence of the moiré pattern superlattices on electronic properties. We apply our approach to the cases of graphene on graphene (G/G) and graphene on hexagonal boron nitride (G/BN), deriving explicit effective Hamiltonians that have the periodicity of the moiré pattern and can be used to calculate electronic properties of interest for arbitrary twist angles and lattice constants.

DOI: 10.1103/PhysRevB.89.205414 PACS number(s): 73.22.Pr, 71.20.Gj, 71.15.Mb, 31.15.aq

I. INTRODUCTION

Since shortly after it was first isolated for electronic property studies in 2004 [1], the graphene family of two-dimensional electron systems has attracted great interest. Recently, attention has expanded [2] to include other extremely anisotropic materials, including hexagonal boron nitride [3] (hBN) and transition metal dichalcogenides [4], and to structures in which combinations of these materials are stacked in various different ways. All these materials share hexagonal lattice structures, and have low-energy electronic states located at momenta near the two-dimensional lattice's Brillouin-zone corners.

Because the lattice constants of these 2D materials differ, and because the hexagonal lattice orientations of different layers are not always identical, multilayer systems usually do not form two-dimensional crystals. For example, the lattice constant of hBN is approximately 1.7% larger than that of graphene. Differences in lattice constant or orientation produce moiré patterns [5] that are apparent in scanning probe studies of electronic properties [6–9] when graphene is placed on a graphite or hBN substrate. The moiré pattern is responsible for Hofstadter [10] gaps [11–14] that occur within Landau levels when samples are placed in a perpendicular magnetic field.

The period of the moiré pattern is unrelated to true two-dimensional crystallinity, which for a given lattice constant difference is present only at discrete relative orientations, and appears to have little relevance for observed properties. The absence of crystallinity nevertheless complicates theoretical descriptions of electronic properties because it removes the simplifications which would otherwise be afforded by Bloch's theorem. This obstacle has forced researchers to proceed either by using simplified tight-binding models [15–19], or by performing *ab initio* or tight-binding calculations [14,20,21] for long-period crystal approximants to real structures. An alternative approach [22–30] is based on the assumption that interlayer tunneling amplitudes in 2D materials vary slowly on an atomic scale with changes in either initial or final two-dimensional position. When this assumption is valid, it is possible to formulate an effective theory of low-energy electronic structure in which the Hamiltonian is periodic with the periodicity of the moiré pattern, and therefore to employ Bloch's theorem. We refer to models of this type, which seek mainly to describe electronic properties in systems with long moiré period structures over a limited energy range, as moiré band models.

In this paper, we extend the moiré band approach, explaining how moiré band models can be systematically obtained from *ab initio* electronic structure calculations performed only on short-period commensurate multilayer structures. The moiré band Hamiltonian is position dependent and acts on real spin and on orbital, sublattice and layer pseudospin degrees of freedom. A moiré band Hamiltonian does not account for the presence or absence of commensurability between the underlying lattices. Moiré band Hamiltonians are particularly advantageous for theories of electronic properties in the presence of an external magnetic field for which other more direct approaches are usually not practical. We illustrate our method of deriving moiré band Hamiltonians by applying it to the case of two graphene layers, and to the case of graphene on hBN.

Our paper is organized as follows. In Sec. II, we explain our approach, which can be applied to any system of layered 2D materials in which the local interlayer stacking arrangement varies slowly on an atomic scale. The parameters of the model can be extracted from *ab initio* electronic structure calculations by examining the dependence of electronic states

on relative displacements between layers in crystalline stacked structures. In Sec. III, we discuss the 2D band structures of crystalline graphene on graphene (G/G) [16–30] and graphene on hexagonal boron nitride (G/BN) [31–38]. We extract the quantitative values of the small number of parameters which characterize the corresponding moiré band models from these calculations. (As experimental results emerge, the model parameters could instead be fit to observed properties if deemed more reliable than *ab initio* electronic structure calculations.) In Secs. III B and III C, we describe applications to G/G and G/BN. For G/BN, it is possible to derive a two-band moiré band model which describes only the graphene layer π bands. We expect that this simplified model, which is explained in Sec. III D, will be widely applicable to evaluate many physical properties of graphene on BN substrates. Finally, in Sec. IV, we summarize our results and briefly discuss some issues which may arise in applying our approach to other 2D material stacks, and in accounting many-body effects that are important for theories of some physical properties.

II. MOIRÉ BAND MODEL DERIVATION

Our method applies to stacks of two-dimensional crystals with the same lattice structure, similar lattice constants, and relative orientation angles that are not too large. It is ideally suited to stacks composed of graphene and hBN layers in arbitrary order with arbitrary orientations, or to group VIB transition-metal dichalcogenide stacks. The basic idea is that the lattice representation Hamiltonian,

$$H_{\rm lat} = \langle ls\vec{L}|H|l's'\vec{L}'\rangle, \tag{1}$$

depends mainly on the local coordination between layers l and l', and that this dependence can be characterized performing calculations for crystalline structures in which the layers are displaced arbitrarily but share the same lattice constant and orientation. In Eq. (1), l labels the layers, each of which is assumed to form a 2D crystal, s labels sites within the 2D crystal unit cell, and $\vec{L}$ labels lattice vectors. If more than one atomic orbital were relevant at each lattice site, as would be the case for transition metal dichalcogenides, for example, s would label both site and relevant orbitals on that site. For graphene and hBN, we will restrict our attention to the π bands so we will consider only one orbital per atom.

The moiré band model is defined by matrix elements of $H_{\rm lat}$ calculated in the representation of the 2D Bloch states of the individual layers. Below, we first explain the approximation we use for $H_{\rm lat}$, and then explain how we use it to evaluate Bloch state matrix elements. We will focus on the case of 2D honeycomb lattices so that our discussion applies specifically to the graphene and hBN cases of primary interest. In this paper, we focus on the two layer case, and comment on the more general case only in the discussion section.

When the individual layer 2D lattices have the same orientation and identical lattice constants, the overall material is crystalline. In that case we can exploit translational symmetry and solve the electronic structure problem using Bloch's theorem. Using Bloch state completeness properties it is easy to show that

$$\langle ls\vec{L}|H(\vec{d})|l's'\vec{L}'\rangle = \frac{1}{N}\sum_{\vec{k}\in BZ} \exp[i\vec{k}\cdot(\vec{L}+\vec{\tau}_s)]\; H_{ls,l's'}(\vec{k}:\vec{d}) \times \exp[-i\vec{k}\cdot(\vec{L}'+\vec{\tau}'_s)]. \tag{2}$$

Here, $H_{ls,l's'}(\vec{k}:\vec{d})$ is the Wannier representation Bloch-band Hamiltonian; we have explicitly indicated that it is a nontrivial function of any rigid displacement $\vec{d}$ of the top layer with respect to the bottom layer. (We include the displacement in the site positions so that $\vec{\tau}_{s'} \to \vec{\tau}_{s'} + \vec{d}$ in the top layer when it is displaced. $\vec{d}$ is defined to be zero for AA stacking.) Note that $\langle ls\vec{L}|H(\vec{d})|l's'\vec{L}'\rangle$ is a function only of $\vec{L}'-\vec{L}$ and not of $\vec{L}$ and $\vec{L}'$ separately, and that $H_{ls,l's'}(\vec{k}:\vec{d}) = H_{ls,l's'}(\vec{k}:\vec{d}+\vec{L})$. The geometry of two stacked honeycomb lattices is illustrated in Fig. 1.

The moiré band model is intended to provide a low-energy effective model of electronic states for the case in which the top layer lattice is expanded by a factor α and rotated counterclockwise by rotation rotation angle θ with respect

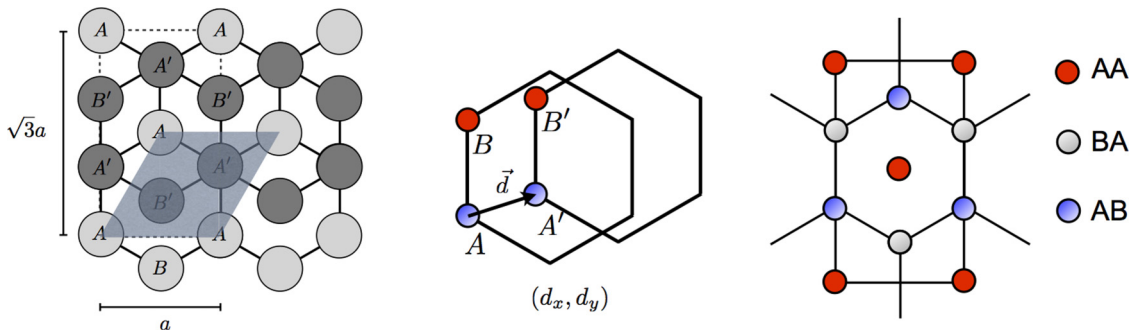

FIG. 1. (Color online) (Left) Schematic representation of two commensurate honeycomb layers with bottom layer sites indicated by light grey circles and top layer sites indicated by dark grey circles. The unit cell of the bilayer contains four sites, A and B for bottom layer and A' and B' for the top layer. The shaded region represents the primitive cell area A_0 used for the Fourier integrals described in the text. (Middle) The relative displacement between the honeycombs is specified by the displacement vector $\vec{d}$. We choose $\vec{d}=0$ for AA stacking in which the two honeycombs have no lateral displacement. For $\vec{d}=(0,a/\sqrt{3})$, we have the AB stacking where the top layer A' site is directly above the bottom layer B site. The bilayer lattice is a periodic function of $\vec{d}$ and the primitive cell for this periodic dependence is shaded grey in the left figure. It is convenient to use the rectangular $a\times\sqrt{3}a$ area enclosed by a dotted line in the left figure to illustrate the dependence of the bilayer Bloch bands on $\vec{d}$. (Right) This panel specifically indicates the points within the rectangular area at which the high symmetry AA, BA, and AB stacking arrangements occur and is helpful for the interpretation of later figures.

to the bottom layer lattice. Note that rigid displacements of incommensurate layers lead only to a spatial shift in the moiré pattern and otherwise have no effect on the electronic structure [22]. When we wish to retain the dependence on initial translation, we denote it by $\vec{\tau}$. For simplicity, we first discuss the case in which $\vec{\tau} = 0$, and later restore the matrix-element phase factor changes introduced by this initial translation. The shift in lattice positions of the top layer with respect to the original positions can then be expressed in terms of α and the rotation operator $\mathscr{R}(\theta)$:

$$\vec{d}(\vec{L}) \equiv \alpha\mathscr{R}(\theta)\vec{L} - \vec{L} = \{[\alpha\cos(\theta) - 1]L_x - \alpha\sin(\theta)L_y, \times [\alpha\cos(\theta) - 1]L_y + \alpha\sin(\theta)L_x\}. \quad (3)$$

We obtain our moiré band model by approximating the lattice matrix elements of the scaled and rotated structure using Eq. (2) with $\vec{d}$ replaced by $\vec{d}(\vec{L})$ in Eq. (3). In using this approximation, we are assuming that $\vec{d}(\vec{L})$ varies slowly on an atomic length scale, i.e., θ and $\alpha - 1 \equiv \varepsilon$ are small. In this limit,

$$\vec{d}(\vec{L}) = \varepsilon\,\vec{L} + \theta\,\hat{z}\times\vec{L}. \quad (4)$$

[The distinction between $\vec{d}(\vec{L})$ and $\vec{d}(\vec{L}')$ is second order in the small parameters ε and θ and therefore neglected. The moiré pattern formed by rotation and scaling is discussed further in Appendix A.] Once this substitution is made, $\langle ls\vec{L}|H(\vec{d})|l's'\vec{L}'\rangle$ depends on both $\vec{L}$ and $\vec{L}'$ and not just on $\vec{L}' - \vec{L}$. It follows that the Hamiltonian is no longer Bloch diagonal in a momentum space representation. Our local displacement approximation is obviously exact for $\varepsilon = \theta = 0$, and we believe that it is accurate over useful ranges of α and θ as discussed further below. We defer further comment on the accuracy of the approximation until we discuss the two explicit examples explored in this paper, G/G and G/BN.

In order to use this approximation conveniently, we note that $H_{ls,l's'}(\vec{k}:\vec{d})$ is a periodic function of $\vec{d}$ with lattice periodicity, i.e., $H_{ls,l's'}(\vec{k}:\vec{d}) = H_{ls,l's'}(\vec{k}:\vec{d}+\vec{L})$. It can therefore be expanded in terms of reciprocal lattice vectors

$$H_{ls,l's'}(\vec{k}:\vec{d}) = \sum_{\vec{G}} H_{ls,l's'}(\vec{k}:\vec{G})\,\exp(-i\vec{G}\cdot\vec{d}) \times \exp[-i\vec{G}(\vec{\tau}_{s'} - \vec{\tau}_s)\widetilde{\delta}_{ll'}]. \quad (5)$$

The phase factor $\exp[-i\vec{G}(\vec{\tau}_{s'} - \vec{\tau}_s)\widetilde{\delta}_{ll'}]$ is included in the definition of the Fourier expansion coefficients in order to make their symmetry properties more apparent, and $\widetilde{\delta}_{ll'} = (1 - \delta_{ll'})$, where l and l' are layer indices. We show below that for G/G and G/BN only a few terms in this Fourier expansion are large. As we explain there, we expect this to be a general property of 2D material stacks.

$H_{ls,l's'}(\vec{k}:\vec{d})$ can be calculated relatively easily by performing *ab initio* supercell density-functional theory (DFT). The number of atoms per unit cell in these calculations is modest, four, for example, in the cases with two crystal layers with two atoms per cell considered explicitly in this paper. The Fourier coefficients which describe the dependence of $H_{ls,l's'}(\vec{k}:\vec{d})$ on $\vec{d}$ are obtained by evaluating the inverse Fourier transform numerically:

$$H_{ls,l's'}(\vec{k}:\vec{G}) = \frac{1}{A_0}\int_{A_0} d\vec{d}\; H_{ls,l's'}(\vec{k}:\vec{d})\exp(i\vec{G}\cdot\vec{d}) \times \exp[i\vec{G}(\vec{\tau}_{s'} - \vec{\tau}_s)\widetilde{\delta}_{ll'}], \quad (6)$$

where A_0 is the integration area of a commensurate configuration primitive cell shown in Fig. 1.

We are now in a position to derive our low-energy model. First of all, we use Eqs. (3) and (5) to construct the momentum space matrix elements of our model. We assume that each layer is still accurately crystalline and for each layer evaluate matrix elements using Bloch states defined using the two-dimensional crystal structure of that layer. Summing independently over the lattice vectors $\vec{L}'$ of layer l' and $\vec{L}$ of layer l and using Eqs. (2), (3), and (5) leads after an elementary calculation to

$$\langle ls\vec{k}|H|l's'\vec{k}'\rangle = \sum_{G} H_{ls,l's'}(\vec{k}:\vec{G})\exp[i\vec{G}\cdot(\vec{\tau}_s - \vec{\tau}_{s'})\widetilde{\delta}_{ll'}] \times \Delta(\vec{k}' - \vec{k} - \tilde{G}), \quad (7)$$

where $\Delta(\vec{k}) = 1$ when $\vec{k}$ is a reciprocal lattice vector and is zero otherwise and

$$\widetilde{G} = \varepsilon\vec{G} - \theta\,\hat{z}\times\vec{G}. \quad (8)$$

In applying this formula, we wish to describe electronic states derived from Bloch orbitals close to a particular or several particular points in momentum space. For graphene and hBN, we wish to describe states close to the Dirac points $\vec{K}$ and $\vec{K}'$. (Below we consider the $\vec{K}$ Dirac point for definiteness.) We further assume that the interlayer coupling processes responsible for $l \neq l'$ and $\vec{G} \neq 0$ terms in Eq. (7) are small compared to the $l = l'$, $\vec{G} = 0$ term, but that they vary with momentum $\vec{k}$ on the same reciprocal lattice vector scale. These assumptions allow us to replace $H_{ls,l's'}(\vec{k}:\vec{G})$ by its value at the Dirac point when $l' \neq l$ or $\vec{G} \neq 0$ to obtain

$$\langle ls\vec{k}|H|l's'\vec{k}'\rangle = \delta_{l,l'}\Big[H_{ls,l's'}(\vec{k}:\vec{G}=0)\delta_{\vec{k},\vec{k}'} + \sum_{\vec{G}\neq 0} H_{ls,l's'}(\vec{K}:\vec{G})\,\Delta(\vec{k}' - \vec{k} - \tilde{G})\Big] + \widetilde{\delta}_{l,l'}\sum_{\vec{G}} H_{ls,l's'}(\vec{K}:\vec{G})\exp[i\vec{G}\cdot(\vec{\tau}_s - \vec{\tau}_{s'})] \times \Delta(\vec{k}' - \vec{k} - \tilde{G}), \quad (9)$$

where the first and second lines are, respectively, the intralayer and interlayer terms.

As we see in Eq. (9), the Hamiltonian is constructed as the sum of several contributions: (i) an isolated layer two-dimensional band structure obtained by averaging over displacements $\vec{d}$, (ii) a sublattice pseudospin dependent term, which acts within layers and accounts for the influence of nearby layers on-site-energies and hopping within layers, and (iii) an interlayer tunneling term, which is also strongly dependent on the local stacking arrangement. The first term in this equation reduces to the isolated layer Hamiltonian

when interlayer coupling is absent. In fact, according to our numerical calculations, the difference between this term and the isolated layer Hamiltonian is negligible for both G/G and G/BN cases. The second and third terms are off diagonal in momentum and therefore account for the moiré pattern which breaks translational symmetry. As we illustrate below, using G/G and G/BN as examples, useful models can be obtained with a small number of independent $H_{ls,l's'}(\vec{K} : \vec{G})$ parameters, partly because of symmetry. The values of the parameters can be evaluated by using *ab initio* electronic structure calculations (the approach we follow in this paper) to examine the relative displacement $\vec{d}$ dependence of the electronic structure of two-dimensional layers that have a common Bravais lattice. Since the basic premises of DFT theory are reasonably reliable for graphene and hBN, the resulting model is expected to capture all qualitative electronic structure features associated with the moiré pattern. More accurate simple models might eventually be achievable by using this approach to construct similar phenomenological models with parameters derived from experimental observations. We illustrate the power of this simple formula below by applying it to the G/G and G/BN cases.

III. *AB INITIO* MOIRÉ BAND MODELS

A. Electronic structure calculations

We calculate our moiré band parameters starting from Wannier-function lattice representations of bilayer perfect crystal Hamiltonians. In this section, we present a brief summary of the first-principles methods employed to obtain the Wannier-function representation Hamiltonian matrices, and discuss some qualitative aspects of the perfect crystal bands of G/G and G/BN that hint at important moiré band properties. Our microscopic calculations were performed for two-layer systems with four atoms per unit cell. We used the software package QUANTUM ESPRESSO [39] that is interfaced with the package WANNIER90 [40,41]. The calculations were performed using a $42 \times 42\,k$-point sampling density, an energy cutoff of 60 Ry, vonBarth-Car norm conserving pseudopotentials, and the Perdew-Zunger LDA parametrization (C,B,N.pz-vbc.UPF). We chose the z-axis repeating cell dimension to be ten times the in-plane lattice constant to suppress the vertical coupling between the repeating cells. The same k-point sampling density was maintained for the Wannier representation construction of the Hamiltonian projected to ten localized orbitals, six corresponding to the σ bonds and four to p_z orbitals centered on the four atoms. The convergence criteria used for self-consistent total energy in the DFT calculations was 10^{-9} eV per unit cell.

Although mirror symmetry is broken in bilayers for general $\vec{d}$, the coupling between π and σ bands is always weak because their energy separation near the Dirac point is $\sim$10 eV, and large compared to coupling matrix elements that are always smaller than 0.1 eV [43]. We therefore retain only the π-electron degrees of freedom in our moiré band models. Because there is only one p_z orbital per carbon atom, the Wannier-representation Hamiltonians discussed below are 4×4 matrices with row and column indices that can be labeled by the four sites in a two-layer crystal. We characterized the dependence on the relative displacement between the layers by performing calculations on a $\vec{d}$-sampling grid with 21×36 points in the $a \times \sqrt{3}a$ area plotted in Fig. 2.

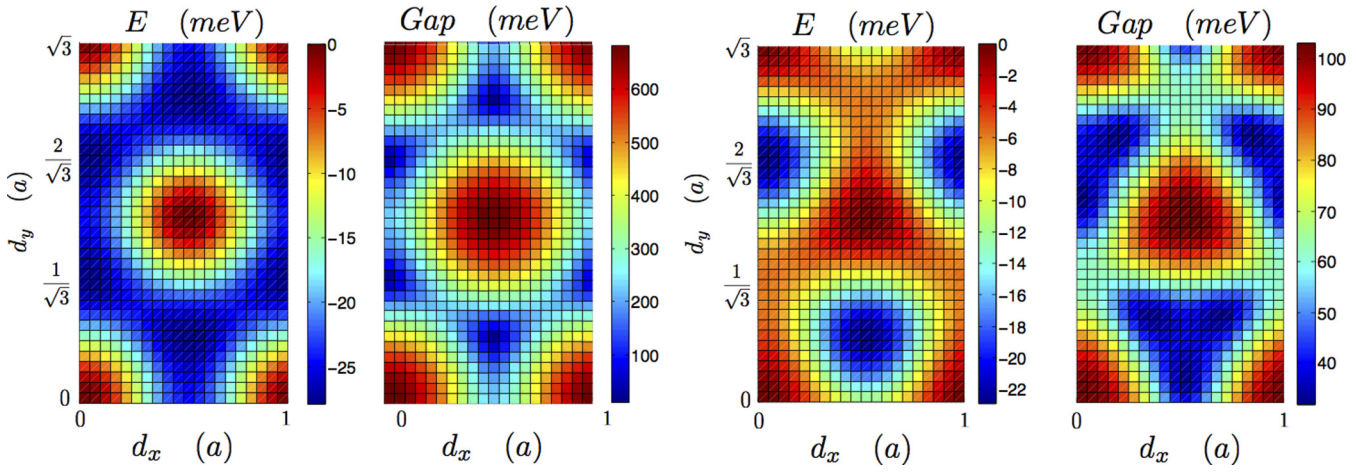

FIG. 2. (Color online) Energy and Dirac point gap landscape as a function of stacking. When the variations are smooth the whole map can be accurately interpolated from the values at the three symmetric stacking points at AA, AB, and BA using Eq. (21) expanded in the first shell of $\vec{G}$ vectors or first harmonic approximation. (Left) Total energy per unit cell relative to AA stacking as a function of displacement $\vec{d}$. These results are for G/G with constant in-plane lattice constant and vertical separation $c = 3.35$ Å. The highest energy configuration corresponds to AA stacking and the lowest to AB or BA stacking. *Gap* refers to the separation between conduction and valence bands at the Dirac point, which vanishes at AB and BA points. (Right) The same plots for G/BN with both sheets constrained to have the in-plane self-consistent LDA lattice constant of graphene and vertical separation $c = 3.35$ Å. The lowest-energy stacking configuration corresponds to BA stacking with one of the two carbon atoms in the graphene unit cell sitting on top of boron. The highest-energy stacking configuration corresponds to the AA arrangement in which the two carbon atoms in the unit cell sit on top of B and N. The AB configuration, which has C on top of N, has an intermediate energy. The scale of the dependence of total energy on $\vec{d}$ is similar in the graphene and hBN cases. Note that the Dirac point gap in the G/hBN case does not vanish at any value of $\vec{d}$, but that the typical gap scale is larger in the G/G case. This later property reflects stronger interlayer coupling.

We have chosen a coordinate system in which graphene's triangular Bravais lattice has primitive lattice vectors

$$\vec{a}_1 = a(1,0), \quad \vec{a}_2 = a\left(-\frac{1}{2}, \frac{\sqrt{3}}{2}\right), \tag{10}$$

where $a = 2.46$ Å is the lattice constant of graphene. The corresponding primitive reciprocal lattice vectors are

$$\vec{b}_1 = \frac{2\pi}{a}\left(1, \frac{1}{\sqrt{3}}\right), \quad \vec{b}_2 = \frac{2\pi}{a}\left(0, \frac{2}{\sqrt{3}}\right). \tag{11}$$

The A and B sublattice positions in the bottom layer are

$$\vec{\tau}_A = (0,0,0), \quad \vec{\tau}_B = \left(0, \frac{a}{\sqrt{3}}, 0\right), \tag{12}$$

and the A' and B' positions in the second layer are

$$\vec{\tau}_{A'} = (d_x, d_y, c), \quad \vec{\tau}_{B'} = \left(d_x, \frac{a}{\sqrt{3}} + d_y, c\right). \tag{13}$$

In Eq. (13), c is the layer separation that we assume to be constant that we normally assume to be 3.35 Å. Results for geometries where the out of plane z direction coordinate is relaxed as function of $\vec{d}$ are discussed in Appendix B.

In Fig. 2, we plot results for the dependence of total energy and the band gap at the Dirac point on displacement $\vec{d}$ for both G/G and G/BN. In the G/BN case, the difference in lattice constant between graphene and hBN layers will play an essential role. The bulk lattice constant of graphite is $a_G = 2.461$ Å whereas $a_{\rm hBN} = 2.504$ Å, implying a difference of about 1.7%. For the commensurate calculations summarized in Fig. 2 we used the self-consistent LDA lattice constant of single layer graphene $a_G = 2.439$ Å for both graphene and boron nitride sheets. Notice that for G/BN there is a gap at the Dirac point at any value of $\vec{d}$.

B. Graphene on graphene

1. *Moiré band model*

In Fig. 3, we illustrate the dependence on $\vec{d}$ of both interlayer and intralayer values of $H_{ls,l's'}(\vec{K} : \vec{d})$ for the case of two-coupled graphene layers. The intralayer parameters are typically ∼5 meV in the graphene case and do not play an essential role in the moiré bands; we will see later that their role is much more essential in the graphene on boron nitride case. The interlayer coupling at the Dirac point is larger and more strongly dependent on $\vec{d}$. As we now explain, a single real parameter is sufficient to accurately describe the full $\vec{d}$ dependence of the four complex interlayer coupling matrix elements. The vast simplification is related to the smooth variation of interlayer coupling on $\vec{d}$, which is related [22] in turn to the fact that the distance between layers of these van der Waals coupled two-dimensional materials is substantially larger than the separation between atoms within a layer.

Figure 4 illustrates typical results of a moiré band parameter calculation performed by using Eq. (6) and integrating over $\vec{d}$. We find that for graphene on graphene the only large corrections to the isolated layer Hamiltonian are for interlayer tunneling, and that these are large at $\vec{G} = 0$ and at two nonzero values of $\vec{G}$, that they are real, and that they are identical in the three cases. The interlayer parameters do not have the symmetry of the reciprocal lattice because they are evaluated at the Brillouin-zone corner Dirac point, rather than at the zone center. The three $\vec{G}$'s, which yield large parameters, share the minimum value of $|\vec{K} + \vec{G}|$. The entire interlayer coupling part of the Hamiltonian is accurately captured by a single real parameter with the value 0.113 ± 0.001 eV. We now explain the physics behind this seemingly surprising simplification.

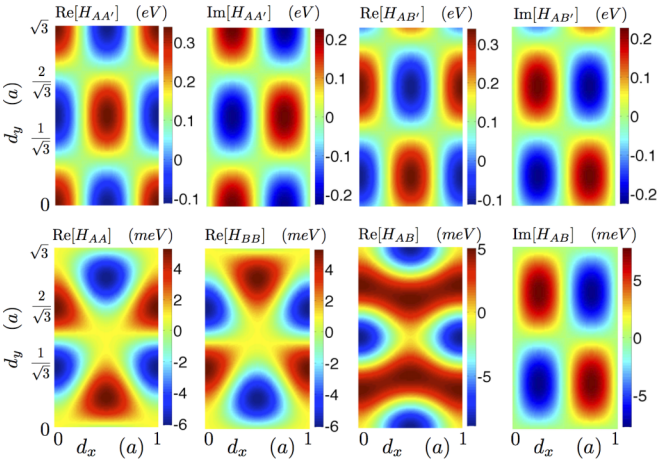

FIG. 3. (Color online) Dirac-point π-band Wannier-representation Hamiltonian matrix elements as a function of sliding vector $\vec{d}$ for graphene/graphene. (Top) Left to right real and then imaginary parts of the AA' and then AB' interlayer matrix elements as a function of position $\vec{d}$ in the rectangular cell of Fig. 1. The BA' matrix element is closely related to the AB' matrix element as shown in Eq. (20) and the BB' matrix element is identical to the AA' matrix element. Interlayer coupling matrix elements have a typical magnitude ∼300 meV. We show later that the dependence of these four complex numbers on $\vec{d}$ is accurately described by a single real number. The color scales show energies in units of eV. (Bottom) Intralayer Wannier-representation Hamiltonian matrix elements. Left to right the real parts of the AA and BB matrix elements followed by the real then imaginary parts of the AB matrix element. Typical matrix element values are ∼5 meV. For graphene on graphene, the spatial variation of intralayer matrix elements has a negligible influence on electronic properties. The color scale shows energy in units of meV.

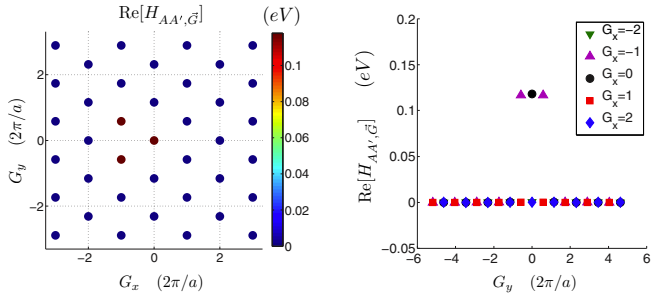

FIG. 4. (Color online) Real part of the Fourier transform of $H_{AA'}(\vec{K} : \vec{d})$ evaluated at $\vec{K} = (4\pi/3a, 0)$. In Fourier space, interlayer coupling is strong only for three reciprocal lattice vectors, $\vec{G} = 0$ and the two nonzero reciprocal lattice vectors for which $|\vec{K} + \vec{G}| = |\vec{K}|$. The imaginary part of $H_{AA'}(\vec{K} : \vec{d})$ vanishes. At these values of $\vec{G}$, $H_{AA'}(\vec{K} : \vec{G})$ is real with identical values of 0.113 ± 0.001 eV.

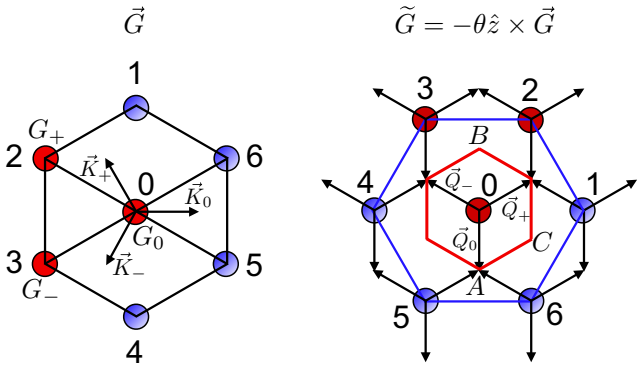

FIG. 5. (Color online) (Left) Representation of the first shell of $\vec{G}$ reciprocal lattice vectors with their corresponding numeral labels used in the main text. The three circles in red correspond to the $\vec{G}_0, \vec{G}_\pm$ vectors with large interlayer tunneling coefficients. The three vectors $\vec{K}_j = \vec{K} + \vec{G}_j$ $j = 0,\pm$ have the same magnitude. (Right) First shell moiré reciprocal lattice vectors $\widetilde{G} = -\theta\hat{z} \times \vec{G}$ for graphene on graphene result differ from the honeycomb reciprocal lattice vectors by a clockwise 90° rotation and a reduction in size by a factor proportional to θ. The solid black arrows represent the $\vec{Q}_j$ vectors that connect a $\vec{q}$ vector in the bottom layer to one in the top layer and the red hexagon encloses the moiré pattern Brillouin zone.

Our low energy model is naturally employed in combination with a continuum model in which wave vectors are measured from the Dirac point. The condition that $\vec{k}' = \vec{k} + \tilde{G}$ then translates into the condition

$$\vec{q}' = \vec{q} + \vec{K} - \vec{K}' + \tilde{G} = \vec{q} + \vec{Q}_j, \tag{14}$$

where $j = 0,\pm$ and the indices correspond to the three $\vec{G}$'s for which $H_{ls,l's'}(\vec{K} : \vec{G})$ is large: $\vec{G} = (0,0)$ and

$$G_\pm = \frac{4\pi}{\sqrt{3}a}\left(-\frac{\sqrt{3}}{2}, \pm\frac{1}{2}\right) = K\left(-\frac{3}{2}, \pm\frac{\sqrt{3}}{2}\right). \tag{15}$$

Here, K is the magnitude of the Dirac wave vector. Taking account of the difference between the rotated and unrotated system reciprocal lattices, we find that to first order in ε and θ

$$\vec{Q}_j = \varepsilon\vec{K}_j - \theta\hat{z} \times \vec{K}_j, \tag{16}$$

where $\vec{K}_j = \vec{K} + \vec{G}_j$. Note that, independent of the values of θ and ε, the three vectors $\vec{Q}_j$ have the same magnitude $K\sqrt{\varepsilon^2 + \theta^2}$ and that they are related by 120° rotations. In the graphene case, the parameter ϵ that accounts for the difference in lattice constant between the layers is equal to zero, but we retain it here because of the close similarity between the G/G interlayer hopping terms and the G/BN cases discussed below. When momenta are measured from the Dirac point, a state in one-layer is coupled to states in the same layer separated in momentum space by moiré pattern reciprocal lattice vectors, and to states in the opposite layers separated by moiré pattern reciprocal lattice vectors $\pm\vec{Q}_j$ (see Fig. 5).

For G/G, the intralayer contribution to the Hamiltonian is negligible for $\vec{G} \neq (0,0)$, and for $\vec{G} = (0,0)$ and $\vec{k} = \vec{K}$, its dependence on site labels is proportional to a unit matrix. It follows that the $\vec{G} = (0,0)$, $\vec{k} = \vec{K}$ Hamiltonian can be set to zero by choosing the zero of energy appropriately. The dependence of the $\vec{G} = (0,0)$ interlayer Hamiltonian on $\vec{k}$ satisfies the same symmetry requirements as the isolated layer Hamiltonian. We have found that for both G/G and G/BN cases, the difference between the $\vec{G} = (0,0)$ interlayer Hamiltonian and the isolated layer Hamiltonian is negligible.

When only the largest nonzero interlayer coupling terms are retained, the Hamiltonian is the sum of three terms, each a product of a coupling constant $t_{\rm bt} = 113$ meV, a momentum boost factor $\delta_{\vec{q}',\vec{q}+\vec{Q}_j}$ and a sublattice dependent factor

$$T^j_{s,s'} = t_{\rm bt}\exp[i\vec{G}_j \cdot (\vec{\tau}_s - \vec{\tau}_{s'} - \vec{\tau})], \tag{17}$$

where we have restored the phase change due to the translation $\vec{\tau}$ prior to rotation. When the momentum boost operator is written in real space, it is local and has a plane-wave spatial dependence. We therefore obtain a Hamiltonian with a space-dependent interlayer coupling Hamiltonian that has a sub lattice pseudospin dependence:

$$H_{\rm bt}(\vec{r}) = \sum_j \exp(-i\vec{Q}_j \cdot \vec{r})\, T^j_{s,s'}, \tag{18}$$

where

$$T^j = t_{\rm bt}\exp(-i\vec{G}_j\vec{\tau})\begin{pmatrix} 1 & \exp(-ij\phi) \\ \exp(ij\phi) & 1 \end{pmatrix} \tag{19}$$

and $\phi = 2\pi/3$. A similar formula was derived previously starting from *ad hoc* π-band tight-binding models [15,22]. (Note that in Ref. [22] the initial displacement τ was defined relative to AB stacking.) This position-dependent interlayer tunneling can be understood in terms of local interlayer coordination which varies with the moiré periodicity between AA, AB, and intermediate arrangements. Here we demonstrate by explicit first-principles calculations that this model for twisted layer electronic structure is quite accurate. Our *ab initio* calculations give rise to a coupling constant of $t_{\rm bt} = 113$ meV, nearly identical to the value $t_{\rm bt} = 110$ meV estimated previously by fitting tight-binding models to the experimentally known Dirac point spectrum of bilayer graphene. In the phenomenological tight-binding model context, the applicability of this model was justified on the basis of the argument [19] that any reasonable interlayer tunneling ansatz yields a dependence on two-dimensional position that is smooth at atomic scale. Our microscopic calculations free us from an *ad hoc* tight-binding model and confirm the expected smoothness. The success of the *ad hoc* tight-binding model in describing interlayer tunneling effects may be traced to the property that only one number, namely $t_{\rm bt}$, is important for the low-energy electronic structure. Any microscopic model, which is adjusted so that it gives an appropriate value for $t_{\rm bt}$, will yield similar predictions.

The explicit form of the $\vec{d}$-dependent interlayer Hamiltonian, which retains only the single strong moiré band model parameter follows from Eq. (5):

$$\begin{aligned}
H_{AA'}(\vec{K} : \vec{d}) &= H_{BB'}(\vec{K} : \vec{d}) \\
&= t_{\rm bt}[1 + \exp(-i\vec{G}_+ \cdot \vec{d}) + \exp(-i\vec{G}_- \cdot \vec{d})], \\
H_{AB'}(\vec{K} : \vec{d}) &= t_{\rm bt}[1 + \exp(-i\phi)\exp(-i\vec{G}_+ \cdot \vec{d}) \\
&\quad + \exp(i\phi)\exp(-i\vec{G}_- \cdot \vec{d})], \\
H_{BA'}(\vec{K} : \vec{d}) &= t_{\rm bt}[1 + \exp(i\phi)\exp(-i\vec{G}_+ \cdot \vec{d}) \\
&\quad + \exp(-i\phi)\exp(-i\vec{G}_- \cdot \vec{d})].
\end{aligned} \tag{20}$$

Although they are relatively weak in the G/G case, for completeness, we specify the leading intralayer terms as well. The Fourier transforms of the intralayer matrix elements have the same magnitude within a shell of reciprocal lattice vectors. Including the first shell only, we obtain the following parametrization of the $\vec{d}$-dependent intralayer Hamiltonian matrix elements:

$$\begin{aligned} H_{ii}(\vec{K}:\vec{d}) &= C_{0ii} + 2C_{ii}\,\mathrm{Re}[f(\vec{d})\exp(i\varphi_{ii})], \\ H_{ij}(\vec{K}:\vec{d}) &= g(C_{ij},\varphi_{ij}) \quad (i \neq j), \end{aligned} \tag{21}$$

where

$$f(\vec{d}) = \exp[-iG_1 d_y] + 2\exp\left(i\frac{G_1 d_y}{2}\right)\cos\left(\frac{\sqrt{3}}{2}G_1 d_x\right), \tag{22}$$

$G_1 = 4\pi/\sqrt{3}a$. The matrix elements labeled by $ii = AA, BB, A'A', B'B'$, are the $\vec{d}$-dependent site energies. The matrix elements labeled by AB and $A'B'$ describe intersublattice tunneling at the Dirac point within the layers. In Eq. (21),

$$\begin{aligned} g(C,\varphi) = {} & 2C\cos\left(\frac{\sqrt{3}G_1}{2}d_x\right)\cos\left(\frac{G_1}{2}d_y - \varphi\right) \\ & - 2C\cos\left(G_1 d_y + \varphi\right) \\ & - i2\sqrt{3}C\sin\left(\frac{\sqrt{3}G_1}{2}d_x\right)\sin\left(\frac{G_1}{2}d_y - \varphi\right). \end{aligned} \tag{23}$$

Using the numerical labels for the $\vec{G}$ vectors in Fig. 5,

$$\begin{aligned} H_{ii,\vec{G}_1} &= H_{ii,\vec{G}_3} = H_{ii,\vec{G}_5} = C_{ii}\exp(i\varphi_{ii}), \\ H_{ii,\vec{G}_2} &= H_{ii,\vec{G}_4} = H_{ii,\vec{G}_6} = C_{ii}\exp(-i\varphi_{ii}) \end{aligned} \tag{24}$$

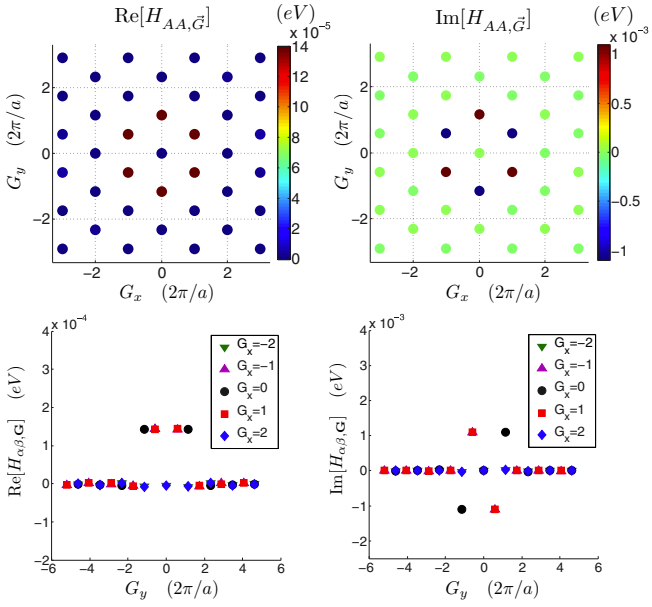

FIG. 6. (Color online) Real and imaginary parts of the Fourier transforms of the intralayer AA site diagonal Hamiltonian matrix element. Because of the symmetries of the honeycomb lattice the $\vec{G}$-dependent site potentials satisfy $H_{AA,\vec{G}} = H^*_{BB,\vec{G}} = H^*_{A'A',\vec{G}} = H_{B'B',\vec{G}}$. These contributions to the twisted layer Hamiltonian for G/G are small and can often be neglected.

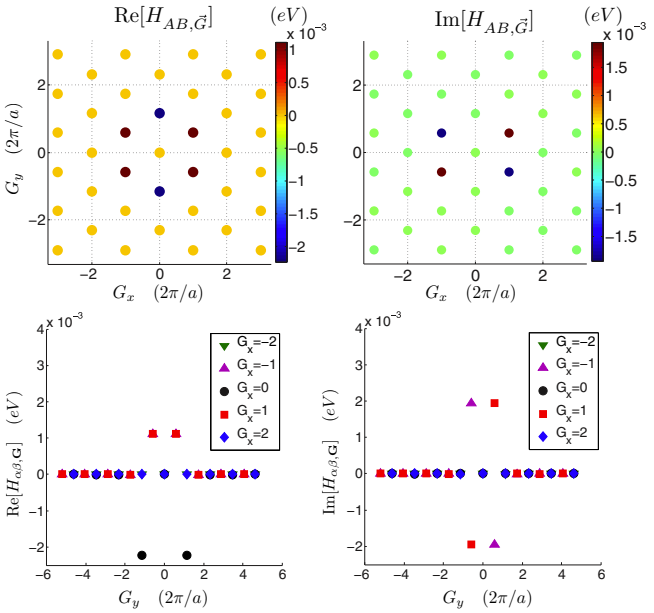

FIG. 7. (Color online) Real and imaginary parts of the Fourier transform of the intralayer, intersubband Hamiltonian matrix element $H_{AB,\vec{G}}$. It follows from symmetry that $H_{AB,\vec{G}} = H_{A'B',\vec{G}}$. These matrix elements are also small.

for the diagonal terms represented in Fig. 6, and

$$\begin{aligned} H_{A^{(\prime)}B^{(\prime)},\vec{G}_1} &= H^*_{A^{(\prime)}B^{(\prime)},\vec{G}_4} = C_{A^{(\prime)}B^{(\prime)}}\exp[i(-\varphi_{AB} - \pi)], \\ H_{A^{(\prime)}B^{(\prime)},\vec{G}_3} &= H^*_{A^{(\prime)}B^{(\prime)},\vec{G}_2} = C_{A^{(\prime)}B^{(\prime)}}\exp[i(-\varphi_{AB} + \pi/3)], \\ H_{A^{(\prime)}B^{(\prime)},\vec{G}_5} &= H^*_{A^{(\prime)}B^{(\prime)},\vec{G}_6} = C_{A^{(\prime)}B^{(\prime)}}\exp[i(-\varphi_{AB} - \pi/3)] \end{aligned} \tag{25}$$

for the off-diagonal terms represented in Fig. 7. For graphene on graphene, the expansion coefficients satisfy the symmetry properties $H_{AA,\vec{G}} = H^*_{BB,\vec{G}} = H^*_{A'A',\vec{G}} = H_{B'B',\vec{G}}$ for the diagonal terms and $H_{AB,\vec{G}} = H_{A'B',\vec{G}}$ for the off diagonal terms, $C_{0AA} = C_{0BB}$, and $\varphi_{AB} = \varphi_{A'B'} = 0$. The numerical values of the nonzero parameters that define the model for G/G are

$$\begin{aligned} & C_{AA} = C_{B'B'} = 1.10\ \text{meV}, \quad \varphi_{AA} = \varphi_{B'B'} = 82.54^\circ, \\ & C_{BB} = C_{A'A'} = C_{AA}, \quad \varphi_{BB} = \varphi_{A'A'} = -\varphi_{AA}, \\ & C_{AB} = 2.235\ \text{meV}. \end{aligned} \tag{26}$$

The sublattice site-energy difference $2H_z(\vec{K}:\vec{d}) = H_{AA}(\vec{K}:\vec{d}) - H_{BB}(\vec{K}:\vec{d})$ vanishes for AA stacking and reaches its maximum value ∼12 meV for the AB stacking configuration. This value is in reasonable agreement with the ∼15 meV site-energy difference estimated elsewhere for AB stacked bilayer graphene [43]. It will be interesting to see if these relatively small terms, which are normally neglected in two-layer graphene systems have any observable consequences. Equation (26) also implies spatial variations of the average site-energy $H_0(\vec{K}:\vec{d}) = (H_{AA}(\vec{K}:\vec{d}) + H_{BB}(\vec{K}:\vec{d}))/2$ that are smaller than 1 meV. These variations will tend to drive small charge transfers between different parts of the moiré pattern, but their role is not especially important because of their small value.

2. First shell approximation for commensurate AB, AA limits

In the following, we test the single-parameter moiré band model in which the interlayer Hamiltonian is truncated at the first shell of its Fourier expansion by applying it to the crystalline AA and AB stacking limits. In the crystalline limit, $\vec{d}$ is independent of position and $\vec{Q}_j = (0,0)$ for $j = 0, \pm$. In the AA stacking configuration, interlayer coupling is maximized because carbon atoms in different layers sit exactly on top of each other. Mirror symmetry leads to layer-symmetric and layer-antisymmetric copies of the single-layer Dirac spectrum. With our conventions, AA stacking corresponds to $\vec{d} = (0,0)$ independent of $\vec{L}$, and to Direct evaluation of the AA Wannier matrix elements yields $H_{AA'}[\vec{K} : \vec{d} = (0,0)] = H_{BB'}[\vec{K} : \vec{d} = (0,0)] = 355$ meV and $H_{AB'}[\vec{K} : \vec{d} = (0,0)] = H_{BA'}[\vec{K} : \vec{d} = (0,0)] = 0$. The matrix element from the Fourier expansion model truncated at the first shell is $3t_{\rm bt} = 339$ meV. For the case of AB stacking $\vec{d} = (0, a/\sqrt{3})$, a direct evaluation of the Wannier matrix elements yields $H_{BA'}[\vec{K} : \vec{d} = (0, a/\sqrt{3})] = 354$ meV, with all other interlayer coupling elements vanishing. (The small difference of 7 meV with respect to the calculation for AB bilayer graphene presented in Ref. [43] is due to the slightly smaller in-plane lattice constants used here.) These comparisons demonstrate that the truncated Fourier expansion single-parameter model yields matrix elements that are are typically inaccurate by ∼15 meV, or by around 5% in relative terms. We emphasize that the truncation at the first shell in the Fourier expansions is not essential to our approach, but is attractive because it yields a model that is specified by a single parameter. The approximate band structures obtained using the above interlayer coupling matrices are compared against the first-principles LDA bands in Fig. 8.

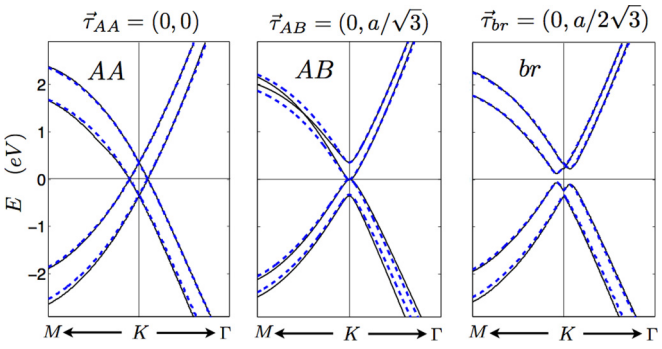

FIG. 8. (Color online) Comparison of LDA G/G band structures (solid lines) and the one-parameter moiré band model (blue dashed lines), which retains only the first shell Fourier-expansion of interlayer coupling. Results are shown for commensurate G/G with AA, AB, and $\vec{\tau}_{\rm br} = (0, a/2\sqrt{3})$ bridge stacking. The electronic structure for BA stacking is identical to AB stacking. We find excellent agreement between the direct and approximate calculations, demonstrating the accuracy of the first shell approximation for interlayer coupling. The intralayer tight-binding Hamiltonian uses the models in Refs. [42,43] with the experimental lattice constants of $a = 2.46$ Å, whereas the interlayer coupling is given by the first shell approximation as parametrized in Eq. (20). The small differences can be attributed mainly to the approximations involved in the first shell approximation for describing the interlayer coupling.

3. Application to twisted bilayer graphene

For G/G, we have $\varepsilon = 0$ so that the moiré pattern reciprocal lattice vectors are related to the honeycomb reciprocal lattice vectors by

$$\widetilde{G} = -\theta\, \hat{z} \times \vec{G}. \tag{27}$$

The Hamiltonian matrix for a given wave vector $\vec{k}$ in the moiré Brillouin zone (MBZ) can be constructed using Eq. (9). The momentum boost operators in the interlayer Hamiltonian terms connect states whose momenta differ by $\vec{Q}_j$, while those in the intralayer Hamiltonian terms connect states whose momenta differ by $\widetilde{G}$. From Eq. (16) the explicit expression for the $\vec{Q}_j$'s is

$$\begin{aligned} \vec{Q}_0 &= \theta K(0,-1), \\ \vec{Q}_+ &= \theta K\left(-\frac{\sqrt{3}}{2}, \frac{1}{2}\right), \\ \vec{Q}_- &= \theta K\left(\frac{\sqrt{3}}{2}, \frac{1}{2}\right). \end{aligned} \tag{28}$$

For every $\vec{k}$ in the MBZ we can construct matrices with 2×2 sublattice blocks. The isolated layer Dirac Hamiltonian contributes blocks that are diagonal in wave vector and layer. The blocks that account for tunneling from bottom to top layers involve momentum boosts by $\vec{Q}_j$, whereas those that connect the same layer involve momentum boosts by a moiré pattern reciprocal lattice vector. Since the $\vec{Q}_j$'s change sign

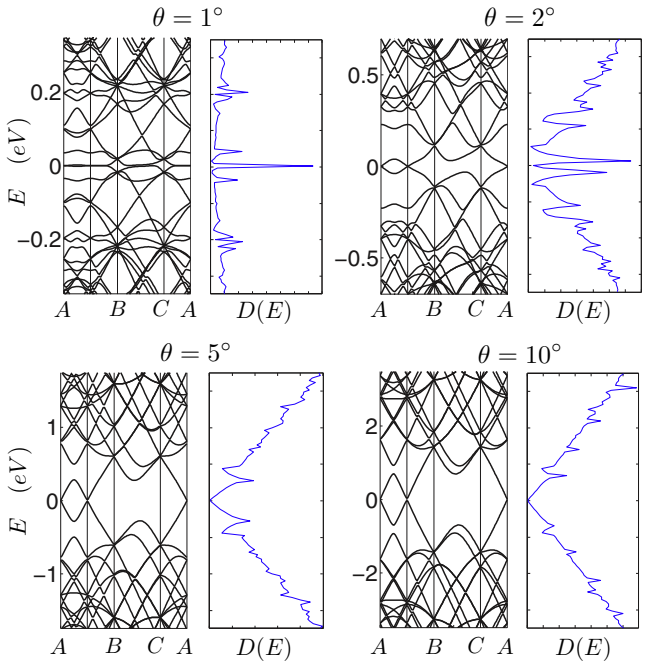

FIG. 9. (Color online) Moiré band structure and density of states of two graphene layers for four different relative orientation angles. Our results are similar to those obtained in Refs. [22,23]. We plot the band structure as a function of momentum along the straight lines in k-space connecting points A, B, C, and A in Fig. 5. The accompanying density-of-states plots demonstrate the complex influence of interlayer coupling, which is responsible for many van Hove singularities.

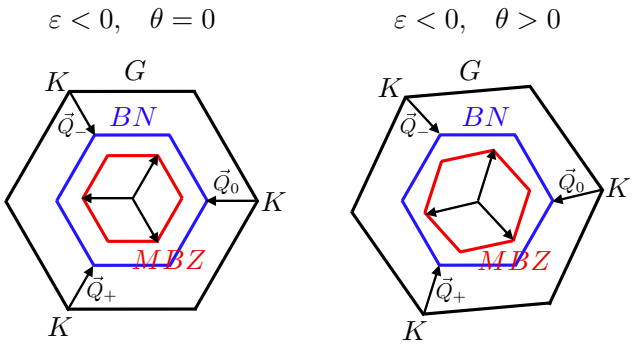

FIG. 10. (Color online) Schematic Brillouin zones of graphene in black lines, of hBN in blue, and the moiré Brillouin zone (MBZ) in red for incommensurate G/BN. The difference between the lattice constants has been exaggerated to aid visualization. Both the size and orientation of the MBZ change continuously with twist angle due to the lattice constant mismatch. The three $\vec{Q}_j$ vectors given in Eq. (16) connect the K points of graphene to those of hBN. The moiré pattern reciprocal lattice vectors can be constructed by summing pairs of $\vec{Q}_j$ vectors.

with tunneling direction, and the difference between any pair of $\vec{Q}_j$'s is a moiré pattern reciprocal lattice vector (see Fig. 5), the crystal momentum defined by the moiré pattern periodicity is a good quantum number. For every $\vec{k}$ in the moiré pattern Brillouin zone, a finite matrix can be constructed by cutting off the plane-wave expansion.

The moiré bands obtained by diagonalizing the matrix constructed in this way are plotted in Fig. 9. We find bands that are similar to those described in Refs. [22,23] in which moiré bands were derived from phenomenological tight-binding models rather than form *ab initio* DFT calculations. The close agreement is expected since both models are accurately approximated by a model with a single interlayer tunneling parameter, as explained above. We now turn to the G/BN case in which the layer coupling effects are more complex. There we will see that our approach, which provides a route to build an effective model based on DFT bands, has distinct advantages over a purely phenomenological approach.

C. Graphene on boron nitride

1. Moiré band model

The crystalline lattices we used to derive the moiré band model parameters for G/BN were identical to those used for the G/G case, except that the bottom layer was changed from graphene to hBN. Because hBN has a slightly larger lattice constant than graphene, the moiré pattern reciprocal lattice vectors are in this case given by the more general expression [Eq. (8)], which accounts for both dilation and twist. The moiré pattern Brillouin zone therefore continuously changes its orientation as a function of twist angle θ as we illustrate in Fig. 10.

In order to capture the local coordination dependence of the electronic structure, we have evaluated Wannier-representation bands over the complete range of interlayer displacement $\vec{d}$ values. The dependence on $\vec{d}$ of Dirac point matrix elements is summarized in Fig. 11. As in the G/G case, these *ab initio* results provide the chemical information that we use to construct a moiré-band model that can account for the lattice constant difference between graphene and hBN, and for the layer orientation difference of particular bilayers. Because these tight-binding model parameters are smooth functions of $\vec{d}$, we can represent them in the moiré band model by a small number of parameters. In Figs. 12–14, we plot moiré band parameters obtained from the information in Fig. 11 using Eq. (6). We find that the $\vec{k}$ dependence of the Hamiltonian (retained only in the $\vec{G} = (0,0)$ moiré band Hamiltonian term calculated by averaging the Wannier representation Hamiltonian over $\vec{d}$) is accurately captured by the Dirac form in both graphene and BN layers.

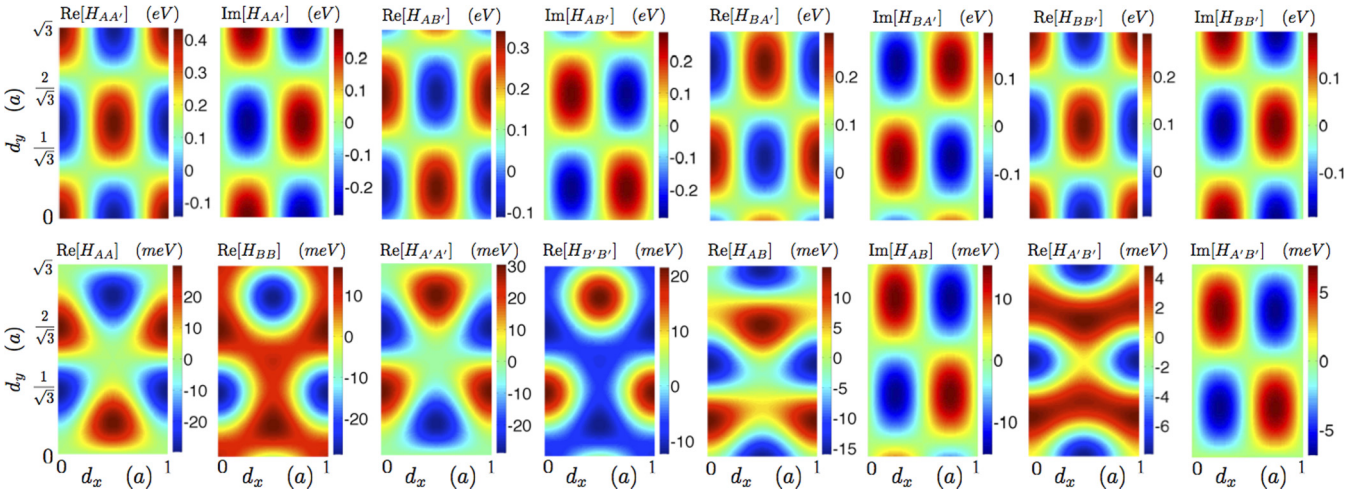

FIG. 11. (Color online) Displacement vector $\vec{d}$ dependence of Wannier representation interlayer Hamiltonian matrix elements for G/BN. (Top) Matrix elements AA', AB' connecting boron with carbon, and matrix elements BA', BB' connecting nitrogen with carbon. The interlayer coupling matrix elements vary over a large range ∼600 meV. (Bottom) Displacement vector $\vec{d}$ dependence of intralayer Wannier representation Hamiltonian matrix elements for G/BN. On-site energies in the graphene layers vary by ∼60 meV. In these plots the site energies are plotted relative to their spatial averages C_{0ii}. [See Eq. (31).] The BN layer AB intersublattice terms vary over a range of ∼35 meV, whereas the graphene layer $A'B'$ terms vary by ∼15 meV.

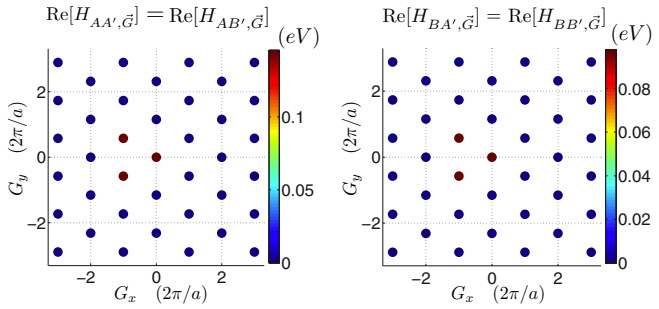

FIG. 12. (Color online) G/BN interlayer moiré band model parameters obtained by evaluating Fourier expansion coefficients for the layer separation dependence of Dirac point Wannier representation Hamiltonian matrix elements. As in the G/G case, three Fourier coefficients dominate interlayer coupling.

The interlayer hopping physics is quite similar in the G/G and G/BN cases. By examining Fig. 11 and comparing with the previous G/G discussion, we conclude that as for G/BN three Fourier coefficients dominate and yield a simple transparent model. Including only these coefficients, we obtain for G/BN,

$$H^{\rm bt}_{s,s'}(\vec{r}) = \sum_j \exp(-i\,\vec{Q}_j\cdot\vec{r})\,T^j_{s,s'}, \tag{29}$$

where

$$T^j = \exp(-i\,\vec{G}_j\vec{\tau})\begin{pmatrix} t_{\rm BC} & t_{\rm BC}\exp(-ij\phi) \\ t_{\rm NC}\exp(ij\phi) & t_{\rm NC}\end{pmatrix}. \tag{30}$$

In this case, there are two distinct interlayer tunneling parameters, which have the values $t_{\rm BC} = 144$ meV and $t_{\rm NC} = 97$ meV. The notation is suggested by comparing these moiré band matrix elements with those constructed from *ad hoc* microscopic tight-binding models [35]. The difference between the boron to carbon and nitrogen to carbon hopping parameters, $t_{\rm BC}$ and $t_{\rm NC}$, is not unexpected since p_z orbitals centered on the boron sites should have larger atomic radii than p_z orbitals centered on the larger Z nitrogen sites. The remaining large contributions to the G/BN moiré band model are absent for G/G and are discussed below.

In the G/BN case, coupling between layers is responsible not only for interlayer tunneling but also for substantial changes within the individual layers. From our microscopic calculations, we find that the carbon site energy parameter is large for the first shell of reciprocal lattice vectors. The momentum space pattern is clearly quite different from that of the interlayer hopping processes. The intralayer Hamiltonian matrix elements can be presented using the same formulas as in Eq. (21) used earlier for the G/G case. What is different in the G/BN case is that our moiré band model is specified by two interlayer tunneling parameters and by 12 intralayer parameters. The values of the 12 intralayer coefficients are listed below:

$$\begin{aligned}
C_{0\,AA} &= 3.332\ \text{eV}, \quad C_{0\,BB} = -1.493\ \text{eV},\\
C_{0\,A'A'} &= 0, \quad C_{0\,B'B'} = 0,\\
C_{AA} &= 5.733\ \text{meV}, \quad \varphi_{AA} = 90^\circ,\\
C_{BB} &= 4.826\ \text{meV}, \quad \varphi_{BB} = 65.49^\circ,\\
C_{A'A'} &= -5.703\ \text{meV}, \quad \varphi_{A'A'} = 87.51^\circ,\\
C_{B'B'} &= -3.596\ \text{meV}, \quad \varphi_{B'B'} = 65.06^\circ,\\
C_{AB} &= 4.418\ \text{meV}, \quad \varphi_{AB} = 26.10^\circ,\\
C_{A'B'} &= 1.987\ \text{meV}, \quad \varphi_{A'B'} = 3.50^\circ.
\end{aligned} \tag{31}$$

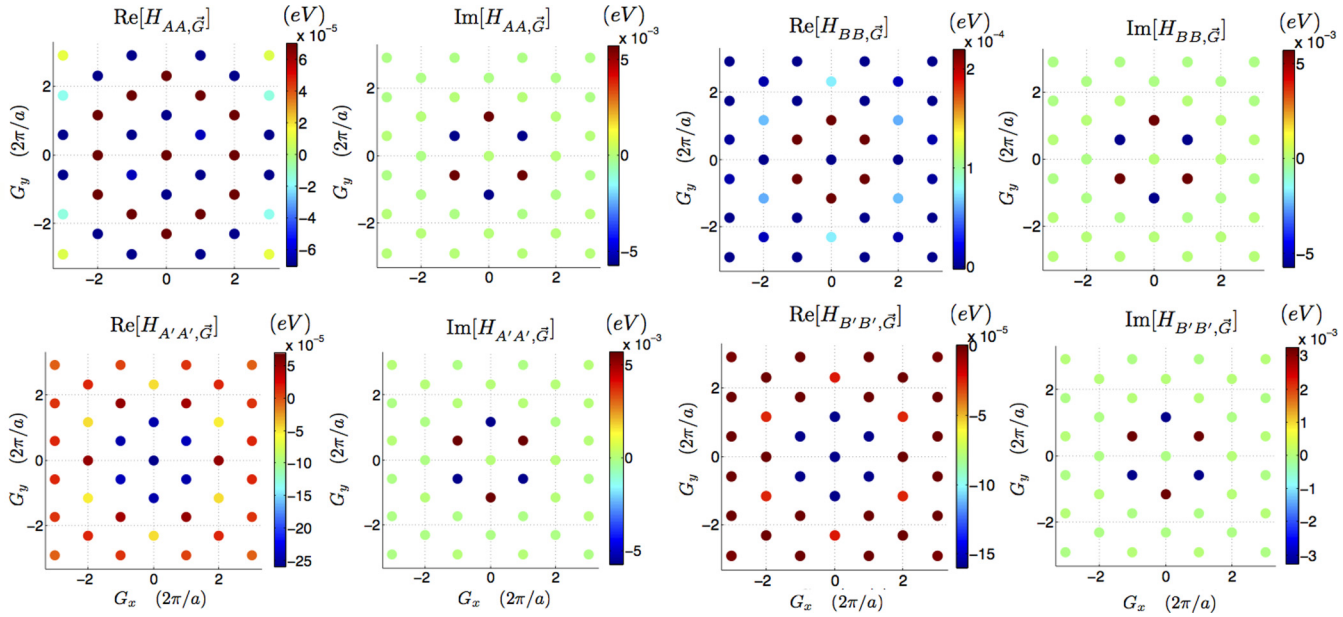

FIG. 13. (Color online) Fourier expansion of the Wannier-representation matrix elements $H_{AA}(\vec{K}:\vec{d})$, $H_{BB}(\vec{K}:\vec{d})$, $H_{A'A'}(\vec{K}:\vec{d})$, and $H_{B'B'}(\vec{K}:\vec{d})$ that describe the interlayer displacement dependence of site-energies in the hBN and graphene layers. These numerical results demonstrate that the site energies are accurately approximated by the model that includes only the first shell of reciprocal lattice vectors. The parameters of this model are listed in the main text. We have chosen the average energy on the carbon sites as the zero of energy. With this choice, the elements corresponding to $\vec{G} = 0$ are $H_{AA}(\vec{K}:\vec{G}=0) = 3.332$ eV for boron, $H_{BB}(\vec{K}:\vec{G}=0) = -1.493$ eV for nitrogen, $H_{A'A'}(\vec{K}:\vec{G}=0) = 0$ eV, and $H_{B'B'}(\vec{K}:\vec{G}=0) = 0$ eV.

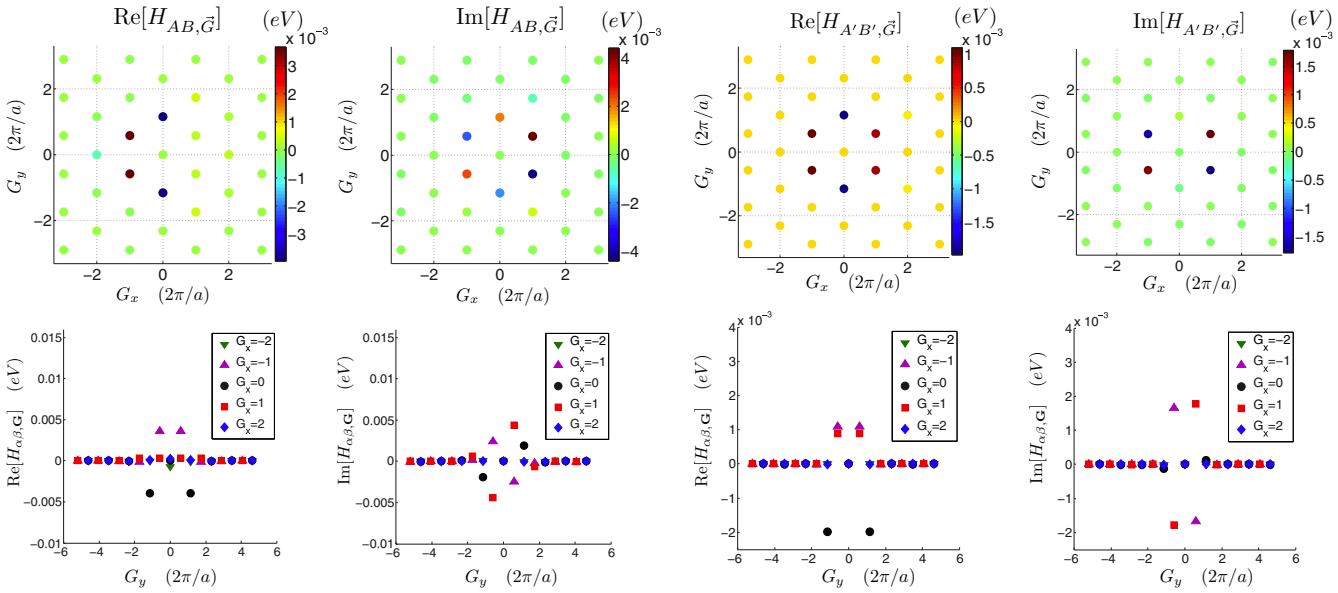

FIG. 14. (Color online) Fourier expansion of the Wannier-representation matrix element $H_{AB}(\vec{K}:\vec{d})$, which describes intersublattice tunneling within the hBN layer, and $H_{A'B'}(\vec{K}:\vec{d})$, which describes intersublattice tunneling within the graphene layer. These numerical results demonstrate that the local coordination dependence of interlayer hopping processes is accurately approximated by the model that includes only the first shell of reciprocal lattice vectors. The parameters of this model are listed in the main text.

The Fourier expansion coefficients of the Hamiltonian can be related with the above set of parameters through the same Eqs. (24) and (25) used in the graphene on graphene case.

2. *First shell approximation for commensurate AA, AB, and BA limits*

In the following, we apply our model Hamiltonian to crystalline AA, AB, and BA stacking limits using the same lattice constant for both graphene and hBN. We proceed with our analysis in a manner similar to the G/G case. The first shell approximation for the commensurate interlayer coupling Hamiltonian closely follows the G/G case, except that it is necessary to distinguish the parameters for tunneling from the boron site and the nitrogen atom site. From Eq. (30) for the AA $[\vec{\tau}_{AA}=(0,0)]$, AB $[\vec{\tau}_{AB}=(0,a/\sqrt{3})]$, and BA $[\vec{\tau}_{BA}=(0,2a/\sqrt{3})]$ stacking configurations, we obtain

$$H_{\rm bt}(\vec{K}:\vec{\tau}_{AA})=3\begin{pmatrix}t_{\rm BC}&0\\0&t_{\rm NC}\end{pmatrix},$$
$$H_{\rm bt}(\vec{K}:\vec{\tau}_{AB})=3\begin{pmatrix}0&0\\t_{\rm NC}&0\end{pmatrix}, \qquad (32)$$
$$H_{\rm bt}(\vec{K}:\vec{\tau}_{BA})=3\begin{pmatrix}0&t_{\rm BC}\\0&0\end{pmatrix}.$$

In the first shell approximation, the tunneling amplitudes are $3t_{\rm BC}=432$ meV and $3t_{\rm NC}=291$ meV respectively. In comparison, direct calculations for these stacking configurations give $H_{AA'}(\vec{K}:\vec{\tau}_{AA})=437$ meV, $H_{BB'}(\vec{K}:\vec{\tau}_{AA})=294$ meV, $H_{BA'}(\vec{K}:\vec{\tau}_{AB})=296$ meV, and $H_{AB'}(\vec{K}:\vec{\tau}_{BA})=439$ meV. The deviations from $3t_{\rm BC}$ and $3t_{\rm NC}$ are in the order of a few meV, which imply relative differences smaller than 2% for the main tunneling terms.

D. Effective low-energy model for G/BN

Our model for the electronic structure of graphene on hBN can be further simplified by formulating a version, which acts only on the low-energy degrees of freedom within the carbon layers. We expect that this version of our model will be broadly applicable to describe electronic properties of graphene sheets that are weakly influenced by a hBN substrate. As we see, the influence will tend to be stronger when the orientation angle difference between graphene and hBN layers is small. In this approach, we integrate out the boron nitride layer degrees-of-freedom to obtain a two-band model for graphene.

When written in terms of 2×2 blocks, the four-band model is given for each $\vec{d}$ by

$$H_{\rm full}=\begin{pmatrix}H_{BN}&T_{BN,G}\\T_{G,BN}&H_G\end{pmatrix}, \qquad (33)$$

where the entries in this matrix are 2×2 matrices that map sub lattices to sub lattices. We choose the zero of energy at the carbon site energies of the graphene layer. The effective Hamiltonian for graphene obtained by integrating out the boron nitride orbitals is

$$H=H_G-T_{G,\,\rm BN}\,H_{\rm BN}^{-1}T_{\rm BN,\,G}. \qquad (34)$$

This expression is valid to leading order in an expansion in powers of the ratio of interlayer tunneling amplitudes to the hBN gap $\sim t_{\rm BN}/(C_{0AA}-C_{0BB})$.

In this two-band model, we can identify four different physical effects of the hBN substrate: (i) there is a $\vec{d}$-dependent difference between the two carbon site energies in the honeycomb unit cell that is absent for an isolated layer. When viewed as a substrate contribution to graphene's two-dimensional Dirac equation $H_z=(H_{A'A'}-H_{B'B'})/2$ can be viewed as a $\vec{d}$-dependent mass. Note that the effective mass

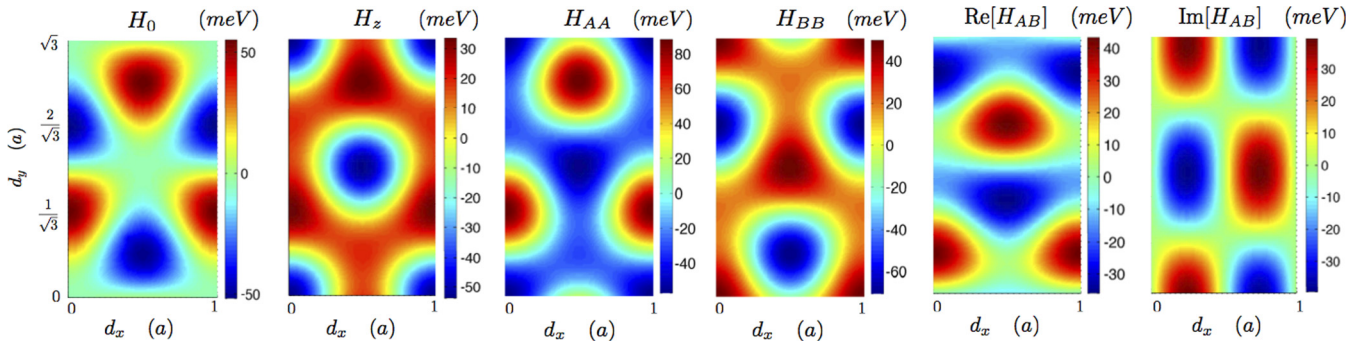

FIG. 15. (Color online) Relative displacement $\vec{d}$-dependence of the matrix elements of the two-band low-energy effective model for graphene on a hBN substrate. In the effective model map the $H_0 = (H_{AA} + H_{BB})/2$ term represents a sublattice independent potential and $H_z = (H_{AA} - H_{BB})/2$ acts as a mass term in the Dirac equation. The off-diagonal matrix-elements H_{AB} accounts for changes in the bonding pattern within the graphene layer. Here, A, B refer to the sublattice sites of graphene.

is sometimes positive and sometimes negative. The A site energy is maximized at AB points, where the carbon A site is on top of a boron atom and far from nitrogen atoms. Similarly, the B site energy is minimized at BA points, where the carbon B site is on top of a nitrogen atom and far from boron atoms. (ii) $H_0 = (H_{A'A'} + H_{B'B'})/2$ can be viewed as a $\vec{d}$-dependent potential term. (iii) $H_{A'B'} = H^*_{B'A'}$ captures the influence of the substrate on hopping between carbon sublattices. This quantity vanishes by symmetry at the Dirac point for an isolated sheet. Our calculations demonstrate that the reduction in symmetry due to the substrate yields a $\vec{d}$-dependent contribution to the Hamiltonian that is roughly of the same size as the mass and potential terms. When the operators that act on sub lattice degrees of freedom are described using Pauli spin matrices, the real part of $H_{A'B'}$ is proportional to the coefficient of σ_x, while the imaginary part is proportional to the coefficient of σ_y. (iv) The final contribution to the effective model is due to virtual occupation of hBN sites and captured by the second term on the right-hand side of Eq. (34). The full effective Hamiltonian can be expanded in terms of Pauli matrices to yield an intuitive representation of the Hamiltonian's sublattice dependence. The term proportional to the identity matrix can be viewed as a potential term, the term proportional to σ_z as a mass term, and the terms proportional to σ_x and σ_y as gauge potentials which account for substrate-induced bonding distortions. Virtual processes contribute to all the effective-model matrix elements discussed above.

The microscopic origin of the mass term can be traced to the difference in electronegativity between nitrogen and boron, which both leads to differences in charging, and modifies the in-plane sigma bonds. Both effects lead to a mass term in the Hamiltonian that is proportional to σ_z. The nitrogen (boron) is negatively (positively) charged. Because the interlayer distance is large, one can crudely approximate the resulting Hartree potential by a Coulomb potential with an effective charge Ze $(-Ze)$ with $0, Z < 1$ acting on the carbon atom just on top of it. This picture has been explored from a phenomenological point of view [35] and gives rise to a mass contribution to the Hamiltonian which is qualitatively similar to the one derived here from first principles.

We construct the moiré band Hamiltonian by letting $\vec{d} \to \vec{d}(\vec{L})$ as explained in Sec. II. The moiré band model is particularly simple when constructed from the two-band effective model:

$$H_{ss'} = H^0_{ss'} + H^{MB}_{ss'}, \tag{35}$$

where $H^0_{ss'}$ is the nonlocal Hamiltonian which describes the Dirac cones,

$$H^0_{ss'} = H_{s,s'}(\vec{k} : \vec{G} = 0)\delta_{\vec{k},\vec{k}'} \tag{36}$$

and $H^{MB}_{ss'}$ is the term which captures the moiré band modulation:

$$H^{MB}_{ss'} = \sum_{\vec{G}\neq 0} H_{s,s'}(\vec{K} : \vec{G})\, \Delta(\vec{k}' - \vec{k} - \tilde{G}). \tag{37}$$

This model can be viewed as the Hamiltonian of graphene subject to external periodic pseudospin-dependent potentials represented in a Fourier expanded form as a sum in the $\tilde{G}$ lattice vectors of the moiré reciprocal lattice. The form of the Hamiltonian is informed by first-principles calculations that account not only for the variation in carbon layer site-energies with local coordination, but also for variations in intercarbon hopping and for virtual hopping between graphene and boron nitride layers. As we will show shortly, thanks to the smooth displacement dependence of the $\vec{d}$-dependent effective Hamiltonian, the moiré patterns of the pseudospin fields are accurately captured by three pairs of parameters, one pair for each pseudospin effective field component. These generalized superlattice potentials determine the quasiparticle velocity and gaps in the moiré superlattice band structure [44]. Our model provides a simple and accurate starting point from which we can calculate the electronic structure of graphene superlattices subject to moiré patterns of the pseudospin fields shown in Figs. 15 and 16.

Our numerical results for the Fourier expansion coefficients of the effective model matrix elements are summarized in Figs. 17 and 18. Once again the expansion coefficients are dominated by the first shell of $\vec{G}$'s, and the number of

independent coefficients is reduced by symmetry. We find that

$$H_0(\vec{K}:\vec{d}) = 2C_0\mathrm{Re}[f(\vec{d})\exp(i\varphi_0)], \quad H_z(\vec{K}:\vec{d}) = 2C_z\mathrm{Re}[f(\vec{d})\exp(i\varphi_z)],$$

$$H_{AB}(\vec{K}:\vec{d}) = 2C_{AB}\cos\left(\frac{\sqrt{3}}{2}G_1d_x\right)\left[\cos\left(\frac{G_1d_y}{2}-\varphi_{AB}\right)+\sin\left(\frac{G_1d_y}{2}-\varphi_{AB}-\frac{\pi}{6}\right)\right]+2C_{AB}\sin\left(G_1d_y+\varphi_{AB}-\frac{\pi}{6}\right)$$
$$+i\,2C_{AB}\sin\left(\frac{\sqrt{3}}{2}G_1d_x\right)\left[\cos\left(\frac{G_1d_y}{2}-\varphi_{AB}\right)-\sin\left(\frac{G_1d_y}{2}-\varphi_{AB}-\frac{\pi}{6}\right)\right]. \quad (38)$$

The site-independent term H_0 gives rise to an overall potential shift in the graphene layer depending on the local stacking order. The pseudospin in-plane terms H_x and H_y together with and the mass term H_z, are the coefficients of σ_x, σ_y, and σ_z in the local 2×2 moiré band Hamiltonian. The in-plane pseudospin terms H_x and H_y can be viewed as a gauge fields $\vec{A}$ [45] that shift the Dirac cone band edges away from the original position. Together these coefficients determine the local Dirac point gap through the relation

$$\widetilde{\Delta}(\vec{r}) = 2\sqrt{H_x^2(\vec{r})+H_y^2(\vec{r})+H_z^2(\vec{r})}. \quad (39)$$

This local Dirac point gap is not directly related to the overall gap of the moiré pattern because of the nonlocality of the momentum-dependent isolated layer Dirac Hamiltonian. (We also expect that the gap will be strongly influenced by many-body effects.) We see in Fig. 16 that the Dirac point gap is everywhere at least 30 meV because H_x, H_y, and H_z do not vanish simultaneously.

Our effective model is completely specified by six numbers:

$$C_0 = -10.13\ \text{meV}, \quad \varphi_0 = 86.53^\circ,$$
$$C_z = -9.01\ \text{meV}, \quad \varphi_z = 8.43^\circ, \quad (40)$$
$$C_{AB} = 11.34\ \text{meV}, \quad \varphi_{AB} = 19.60^\circ.$$

As described in detail for the G/G case, wave vector reduced to the moiré Brillouin-zone is a good quantum number for this model, and band eigenstates may be obtained by making plane-wave expansions. The graphene layer Dirac Hamiltonian contributes to diagonal blocks in the plane-wave representation of the moiré band Hamiltonian. The Fourier expansion of the Hamiltonian in $\vec{G}$ vectors can be related to the above parameters through Eq. (24) for the diagonal terms, either in the pseudospin or sublattice basis, and for the off-diagonal terms shown in Fig. 18, we have the following form:

$$H_{AB,\vec{G}_1} = H^*_{AB,\vec{G}_4} = C_{AB}\exp[i(2\pi/3-\varphi_{AB})],$$
$$H_{AB,\vec{G}_3} = H^*_{AB,\vec{G}_2} = C_{AB}\exp(-i\varphi_{AB}), \quad (41)$$
$$H_{AB,\vec{G}_5} = H^*_{AB,\vec{G}_6} = C_{AB}\exp[i(-2\pi/3-\varphi_{AB})].$$

The applicability of the effective model is evidenced by its accuracy in describing the band structure for the commensurate stacking arrangements shown in Fig. 19. In these plots, local potential fluctuations due to H_0 are manifested by a small offset between the graphene and hBN bands. In the presence of a finite twist angle, the H_0 term leads to an effective potential that varies in space as shown in Fig. 20. These potential variations on the Moire pattern scale leads to the local density-of-state variations seen experimentally [9] and will lead in general to contrasting local density of states at the different vertices of the triangular superlattices.

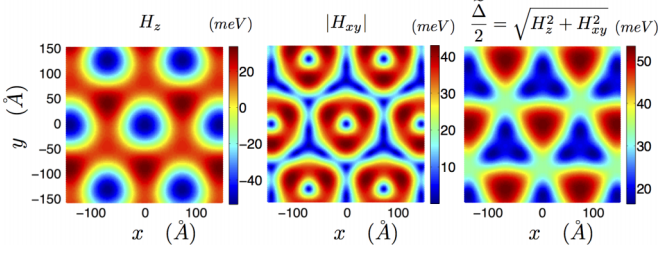

FIG. 16. (Color online) Mass and pseudospin field terms in the effective Hamiltonian as a function of displacement $\vec{d}$. The H_z term is due to sublattice potential difference and vanishes along lines of this two-dimensional plot. The simultaneous presence of finite H_x and H_y and H_z terms in the effective Hamiltonian implies that the Dirac-point gap [Eq. (39)] does not vanish at any relative displacement.

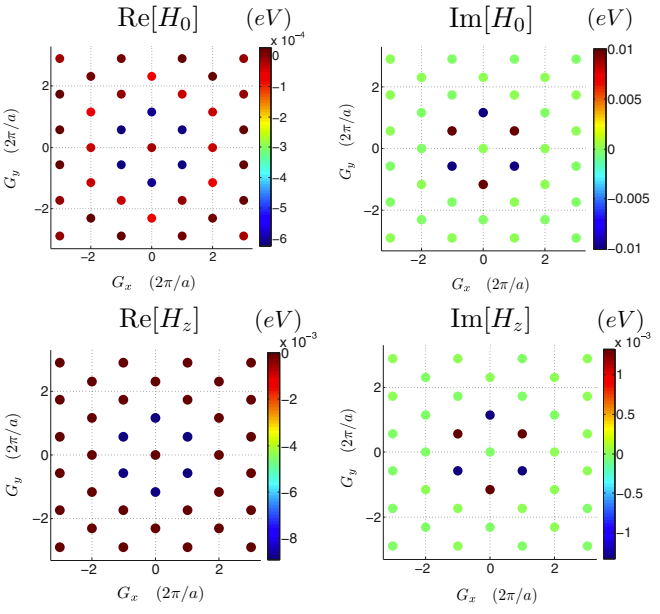

FIG. 17. (Color online) (Top) Fourier expansion coefficients for the effective model matrix element $H_0(\vec{K}:\vec{d})$. This term captures the variation of the site-averaged potential across the moiré pattern. The first shell of reciprocal lattice vectors dominates. (Bottom) Fourier expansion coefficients for the mass term in the effective model, $H_z(\vec{K}:\vec{d}) = [H_{AA}(\vec{K}:\vec{d}) - H_{BB}(\vec{K}:\vec{d})]/2$.

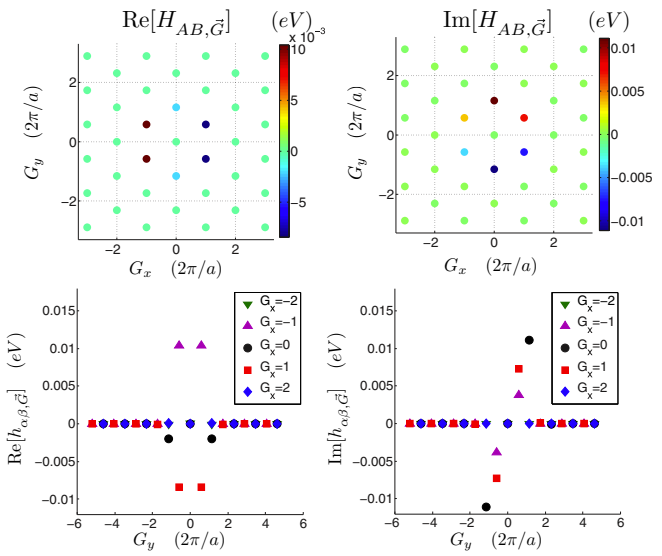

FIG. 18. (Color online) Fourier expansion coefficients for the off diagonal effective model matrix element $H_{AB}(\vec{K} : \vec{d})$. The first shell of reciprocal lattice vectors dominates.

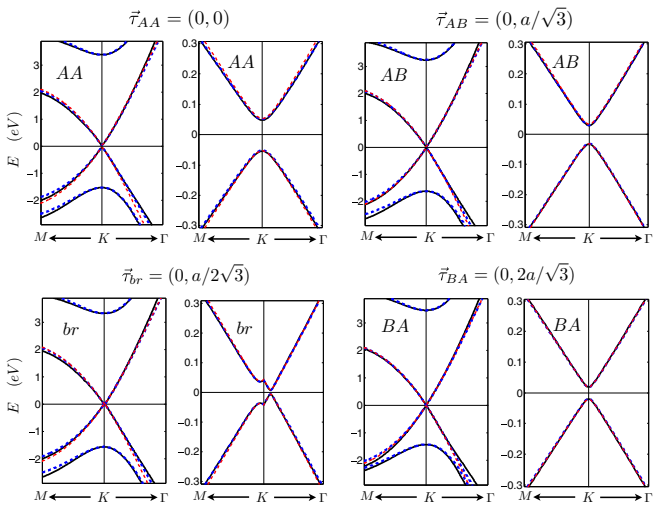

FIG. 19. (Color online) Comparison of the LDA band structure (solid black), the four-band moiré band model (dashed blue lines) and the low energy two-band model (dashed red lines) with the first shell used for the superlattice potentials. The commensurate G/BN arrangements plotted are AA, AB, BA, and a bridge stacking with $\vec{\tau}_{\rm br} = (0, a/2\sqrt{3})$. Note that he electronic structures of AB and BA stacking are different in the G/B case. For the intermediate bridge stacking we see a substantial reduction of the band gap due to a shifting in the Dirac cone momentum space location caused by in-plane pseudospin terms. The intralayer Hamiltonian of graphene is approximated using the massless Dirac model with the LDA Fermi velocity [42] while the boron nitride Hamiltonian is modeled with the same Dirac model with a mass term compatible with the LDA gaps. The interlayer coupling is given by the first shell approximation using the parametrizations of Eq. (20), with tunneling from boron and carbon sites distinguished as in Eq. (30) and the parameter set in Eq. (31). In these plots, the energy origin of the represented bands has been adjusted so that zero is in the middle of the band gap.

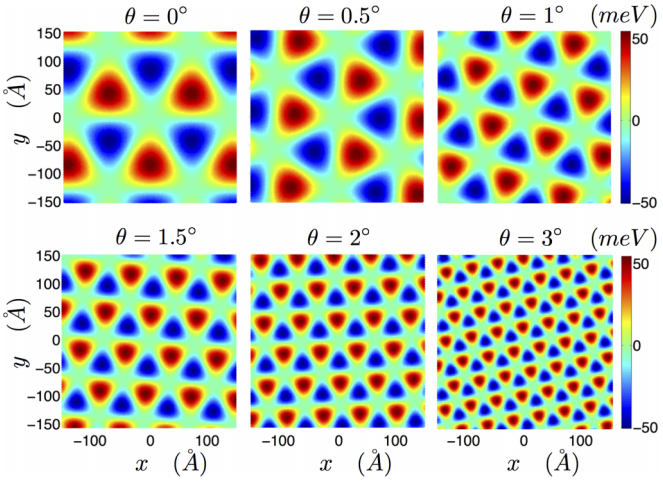

FIG. 20. (Color online) Modulation of the local potential fluctuations $H_0(\vec{r})$ in real space for different twist angles. These plots illustrate the rotation of the moire pattern when $|\varepsilon| \sim \theta$, and the property that the Moire periodicity $L_M \sim a/\sqrt{\varepsilon^2 + \theta^2}$ becomes shorter with increasing twist angle. The other pseudospin components of the local Hamiltonian illustrated Fig. 15 produce similar spatial superlattice patterns.

Even when a graphene sheet on a hBN substrate is globally neutral the charge density will vary locally. The regions within the moiré pattern in which positive and negative charge densities are expected can be identified by neglecting the nonlocal Dirac Hamiltonian (which vanishes at the Dirac point) and the H_x and H_y sublattice coupling terms. In this limit, charge puddles should be expected wherever the chemical potential, set by imposing global charge neutrality, lies below the lower sublattice site energy or above the upper sub lattice site energy. Since the chemical potential at neutrality is very close to the average site energy, which we have chosen as the energy zero, this condition for the formation of charge puddles is equivalent to $|H_0(\vec{r})| > |H_z(\vec{r})|$, with the carrier type

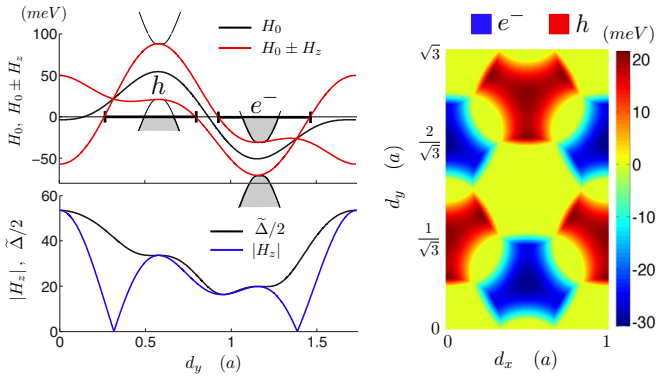

FIG. 21. (Color online) (Left) Schematic illustration of potential variations and local band edges as a function of d_y for fixed $d_x = 0$. The approximate conditions for local electron/hole charging discussed in the main text are satisfied over the segments identified by bold black lines. The difference between the Dirac point gap $\tilde{\Delta}$ and the absolute value of the mass $|H_z|$ reflects the influence of the in-plane pseudospin fields terms. (Right) Sliding vector $\vec{d}$ dependent map of electron and hole puddles.

being electrons if $H_0 > H_z$ and holes if $H_0 < H_z$. In Fig. 21, we apply this criterion to obtain a map of electron and hole puddles from the parametrization for H_0 and H_z presented in Eq. (38). To obtain a more quantitatively accurate map it will be necessary to restore the H_x and H_y and to take into account other effects such as the electrostatic screening and many-body corrections. Lattice relaxations, whose influence is discussed in the Appendix, will also play a role.

IV. SUMMARY AND DISCUSSION

We have presented a method which can be used to derive approximate electronic structure models for layered semiconductors, semimetals, and gapless semiconductors containing a finite number of two-dimensional crystals with different lattice constants and/or different crystal orientations. The method is intended to be useful for multilayer graphene systems, multilayer transition metal dichalcogenide systems, and for multi-layer systems containing both graphene and boron nitride. When several layers are present simultaneously, structures of this type are not in general two-dimensional crystals, and electronic structure theory can therefore be awkward to apply directly because Bloch's theorem is not valid.

Our approach focuses on the influence on the electronic structure of slowly varying relative displacements $\vec{d}(\vec{L})$ between individual crystalline layers due to a small difference in lattice constants or crystal orientations. The dependence of electronic structure on $\vec{d}$ can be calculated without experimental input using density-functional theory. Our analysis produces a moiré band model that is periodic under translations $\vec{R}$ for which

$$\vec{d}(\vec{L}+\vec{R}) = \vec{d}(\vec{L}) + \vec{L}' \tag{42}$$

for some two-dimensional lattice vector $\vec{L}'$. The system is microscopically crystalline only if the vectors $\vec{R}$ for which Eq. (42) is satisfied are lattice vectors of the two-dimensional crystal. The vectors $\vec{R}$ are the lattice vectors of the moiré pattern. Like the moiré pattern itself [7], our moiré band models have a periodicity defined by spatially varying layer alignment, and can therefore be analyzed using Bloch's theorem for a superlattice Hamiltonian that has the periodicity of the moiré pattern. The models consists of massless or massive Dirac models for each two-dimensional layer, combined with a spatially local effective potential which acts on sublattice degrees of freedom.

Our approach to coupled bilayer systems has three main limitations. First of all, it does not apply to cases in which differences in lattice constants or rotation angles between adjacent layers are large. This limitation can be overcome, however, by building a theory that is based on larger unit cells with more sublattice sites and lattice constant ratios between neighboring layers closer to one. For example, for G/G, one could, for example, build models that are similar to the ones discussed here which would apply at rotation angles close to the short-period commensurate rotation angles. Secondly, because it attempts to describe bands over a relatively small part of the Brillouin zone, it is valid over a limited energy range. Finally, it assumes that the individual layers are indeed crystalline whereas we should in fact expect that the moiré pattern will induce small structural distortions within each layer. For the van der Waals epitaxial systems of interest, however, it seems reasonable to expect these distortions to be small and to neglect them, at least as a first approximation.

We have applied our moiré band method to two different two-layer systems, one with two graphene layers and one with a graphene layer and a hexagonal boron nitride layer. For the case of graphene on boron nitride, which has a large energy gap, we have also derived a simpler model, specified by Eqs. (35) and (40), in which the boron nitride degrees of freedom are treated perturbatively to obtain an explicit model for graphene on a boron nitride substrate which retains only the graphene π-electron degrees of freedom. In the case of graphene on graphene, our calculations explain why the dependence on relative orientation angle of G/G electronic structure is accurately described by a model with a single-interlayer tunneling parameter. For the case of graphene on boron nitride, the models we produce are more complicated because of the need to account for the dependence on $\vec{d}$ of graphene-layer site energies and interlayer tunneling amplitudes, but still have a small number of parameters. Nevertheless, the graphene only model for G/BN is able to accurately describe the dependence of low-energy bands on rotation angle using six parameters, which we have calculated from the $\vec{d}$ dependence of *ab initio* bands.

The models derived in this paper can be used as a starting point to account for the influence of either graphene or hBN substrates on the electronic structure of a graphene layer. We expect that they will be applicable to examine a wide variety of electronic properties. Because our models are derived from LDA band structures, they do not account for the nonlocal exchange and correlation effects which are known to be responsible for large Fermi velocity enhancements in isolated graphene systems [46]. The same effects are likely to be important in multi-layer systems, possibly enhancing band gaps produced by the moiré pattern potentials [47]. Our electronic structure models are sufficiently simple that important many-body physics effects can be addressed separately where they play an essential role.

ACKNOWLEDGMENTS

This work was supported by the Department of Energy, Office of Basic Energy Sciences under contract DE-FG02-ER45118, and by Welch Foundation grant TBF1473. JJ was partially supported by the National Research Foundation of Singapore under its Fellowship program (NRF-NRFF2012-01). Z.Q. is also financially supported by USTC Startup, Bairen Program of Chinese Academy of Sciences and NNSFC (Grant No. 91021019). Helpful conversations with Rafi Bistritzer and Byounghak Lee are gratefully acknowledged. We appreciate assistance and computer time provided by the Texas Advanced Computing Center.

APPENDIX A: EXACT FORM OF THE DISPLACEMENT VECTOR AND MOIRE RECIPROCAL LATTICES

In the main text, we used the small angle approximation for the displacement vectors and the moire reciprocal lattices. These approximations are accurate for rotations angles $\theta \simeq 15^\circ$. Here we present the exact form of the lattice vector scaling and rotation transformation and the moire reciprocal lattice

vectors. Let us consider the rotation operator

$$\mathscr{R}(\theta) = \begin{pmatrix} \cos\theta & -\sin\theta \\ \sin\theta & \cos\theta \end{pmatrix} \tag{A1}$$

and write the local displacement vector as

$$\vec{d}(\vec{L}) = \alpha\mathscr{R}(\theta)\vec{L} - \vec{L} = (\alpha\mathscr{R}(\theta) - 1)\vec{L} = \widetilde{\mathscr{R}}(\alpha,\theta)\vec{L}, \tag{A2}$$

where we have defined a new transformation operator $\widetilde{\mathscr{R}}(\alpha,\theta)$, α is the scaling ratio and θ is the twist angle of the top layer with respect to bottom layer. The magnitude β is the scaling factor associated to the transformation

$$|\widetilde{\mathscr{R}}(\alpha,\theta)\vec{L}| = \beta|\vec{L}|, \tag{A3}$$

where $\beta = [\varepsilon^2 + (1+\varepsilon)(2-2\cos\theta)]^{1/2}$ was approximated in the main text as $\sim(\varepsilon^2+\theta^2)^{1/2}$ when we neglected the higher-order corrections.

The moire reciprocal lattice vectors $\widetilde{G}$ can be obtained applying the adjoint of the transformation operation $\mathscr{R}(\alpha,\theta)$ on the $\vec{G}$ vectors

$$\begin{pmatrix} \widetilde{G}_x \\ \widetilde{G}_y \end{pmatrix} = \begin{pmatrix} \alpha\cos\theta - 1 & \alpha\sin\theta \\ -\alpha\sin\theta & \alpha\cos\theta - 1 \end{pmatrix}\begin{pmatrix} G_x \\ G_y \end{pmatrix} \tag{A4}$$

$$= \beta\begin{pmatrix} \cos\widetilde{\theta} & -\sin\widetilde{\theta} \\ \sin\widetilde{\theta} & \cos\widetilde{\theta} \end{pmatrix}\begin{pmatrix} G_x \\ G_y \end{pmatrix}. \tag{A5}$$

We defined the rotation angle $\widetilde{\theta}$ of the moire reciprocal lattice vectors with respect to the original $\vec{G}$ vectors and they can be obtained from the relations

$$\widetilde{\theta} = \cos^{-1}[(\alpha\cos\theta - 1)/\beta], \tag{A6}$$

$$\widetilde{\theta} = \sin^{-1}(-\alpha\sin\theta/\beta). \tag{A7}$$

APPENDIX B: INFLUENCE OF VERTICAL LATTICE CONSTANT RELAXATION

In this Appendix, we present another set of model parameters obtained allowing lattice relaxation for the interlayer distance in the self-consistent LDA calculations, instead of fixing the vertical atomic separations at the experimental interlayer spacing $c = 3.35$ Å of graphite. Even though the LDA approximation does not accurately capture the nonlocal van der Waals type interlayer interactions that are important in these systems, its tendency to over-bind covalent bonds allows it to hold the weakly interacting layers together, and describe the interlayer lattice constants and the forces between van der Waals layered materials reasonably well. LDA results tend to have reasonable agreement with sophisticated RPA and beyond total energy calculations for thin jellium metal slabs [48], hexagonal boron nitride [49], and graphite [50] and other layered materials [51]. We allowed relaxation of the atomic positions in the out of plane z direction using the same 42×42 k-point grid and using a slightly coarser threshold of total energy convergence in the geometry relaxation of 10^{-8} a.u. per unit cell and total force of 10^{-7} a.u. In both G/G and G/BN cases, the overall effect of the relaxation is to increase the interlayer separation by $\sim$0.2 Å with respect to the closest interlayer separation. These changes leads to a weakening of the interlayer coupling strength in the first shell approximation by about 7%, which implies that farther $\vec{G}$ vectors in the Fourier expansion become more important. The changes in the position of the Fermi energy with respect to the unrelaxed geometry are in the order of $\sim$10 meV for G/G and $\sim$30 meV for G/BN providing a measure of changes in the shifts in the site potential offsets between the layers near the AA stacking configurations that are incorporated in the relaxed parameter set. Because the pseudopotentials are referenced to vacuum this information gives an estimate of the modulation in the work function of the graphene sheet due to its coupling with the hBN layer. The above observations suggest that geometry relaxation can introduce small but non-negligible changes in the potential map and details of valence-conduction bands overlap in the G/BN case whose band structure near the Fermi energy is determined simultaneously by in-plane xy and z pseudospin terms of comparable magnitudes. This and other details of the electronic structure in a G/BN heterostructure will be presented elsewhere.

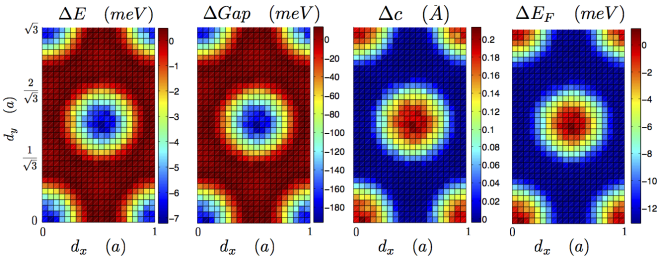

FIG. 22. (Color online) Changes in total energy, Dirac point gaps, average layer separation distance, and Fermi energy resulting from allowing self-consistent LDA relaxation in the out of plane z axis for G/G.

1. Relaxed geometry parameters for G/G

The $\vec{d}$-vector dependent maps of the Hamiltonian matrix elements are changed only quantitatively relative to the unrelaxed case, see Fig. 22. The numerical values of the parameters that define the intralayer model for G/G in Eq. (21) for relaxed geometries are

$$\begin{aligned} C_{AA} &= 2.3 \text{ meV}, \quad \varphi_{AA} = 27.5^\circ, \\ C_{BB} &= C_{AA}, \quad \varphi_{BB} = -\varphi_{AA}, \\ C_{AB} &= 2.08 \text{ meV}, \end{aligned} \tag{B1}$$

whereas the interlayer tunneling constants are $t_{\text{bt}} = 98$ meV. The average interlayer separation distance lies between the

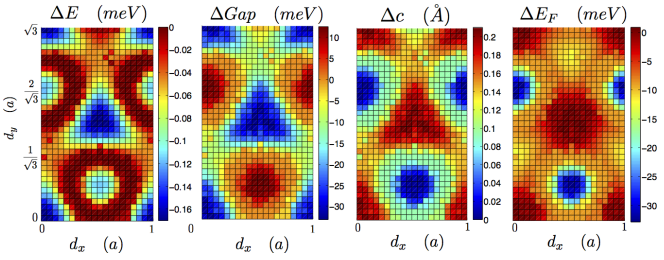

FIG. 23. (Color online) Changes in total energy, Dirac point gaps, average layer separation distance measured from the minimum separation distance, and Fermi energy resulting from allowing self-consistent LDA relaxation in the out of plane z axis for G/BN.

minimum 3.347 Å and the maximum of 3.563 Å for AA stacking.

2. Relaxed geometry parameters for G/BN

For G/BN, we have kept the coordinates fixed for the BN sheet, while we allowed the carbon atoms to relax in the out of plane direction as a function of $\vec{d}$. T The $\vec{d}$-vector dependent map of the Hamiltonian matrix elements for G/BN for relaxed geometries also has some quantitative changes relative to the unrelaxed calculations, see Fig. 23. The numerical values of the parameters that define the intralayer model for G/BN together with the Eqs. (21) for relaxed geometries are

$$\begin{aligned} C_{0AA} &= 3.334 \text{ eV}, \quad C_{0BB} = -1.494 \text{ eV}, \\ C_{0A'A'} &= 0, \quad C_{0B'B'} = 0, \\ C_{AA} &= 5.643 \text{ meV}, \quad \varphi_{AA} = 56.37^\circ, \\ C_{BB} &= 4.216 \text{ meV}, \quad \varphi_{BB} = 59.98^\circ, \\ C_{A'A'} &= -7.402 \text{ meV}, \quad \varphi_{A'A'} = 77.71^\circ, \\ C_{B'B'} &= -4.574 \text{ meV}, \quad \varphi_{B'B'} = 85.78^\circ, \\ C_{AB} &= 4.01 \text{ meV}, \quad \varphi_{AB} = 22.2^\circ, \\ C_{A'B'} &= 1.90 \text{ meV}, \quad \varphi_{A'B'} = 1.30^\circ, \end{aligned} \tag{B2}$$

whereas the interlayer tunneling constants are $t_{\text{BC}} = 130$ meV and $t_{\text{NC}} = 87$ meV. The average interlayer separation distance lies between 3.256 Å and the maximum of 3.466 Å for AA stacking. The parameters of the effective model of G/BN for the relaxed geometries in the sublattice basis are given by

$$\begin{aligned} C_{AA} &= -13.3 \text{ meV}, \quad \varphi_{AA} = 63.63^\circ, \\ C_{BB} &= 14.0 \text{ meV}, \quad \varphi_{BB} = -51.27^\circ, \\ C_{AB} &= 9.53 \text{ meV}, \quad \varphi_{AB} = 21.82^\circ. \end{aligned} \tag{B3}$$

The parameters in the sublattice basis and in the pseudospin basis can be related through

$$\begin{aligned} C_{AA} &= -\sqrt{C_0^2 + C_z^2 - 2C_0C_z\cos(\varphi_0 - \varphi_z)}, \\ \varphi_{AA} &= \tan^{-1}\left[\frac{C_0\sin(\varphi_0) - C_z\sin(\varphi_z)}{C_0\cos(\varphi_0) - C_z\cos(\varphi_z)}\right], \\ C_{BB} &= \sqrt{C_0^2 + C_z^2 + 2C_0C_z\cos(\varphi_0 - \varphi_z)}, \\ \varphi_{BB} &= \tan^{-1}\left[\frac{C_0\sin(\varphi_0) + C_z\sin(\varphi_z)}{(C_0\cos(\varphi_0) + C_z\cos(\varphi_z)}\right]. \end{aligned} \tag{B4}$$

[1] K. S. Novoselov, A. K. Geim, S. V. Morozov, D. Jiang, Y. Zhang, S. V. Dubonos, I. V. Grigorieva, and A. A. Firsov, Science **306**, 666 (2004).

[2] K. S. Novoselov, Rev. Mod. Phys. **83**, 837 (2011).

[3] C. R. Dean, A. F. Young, I. Meric, C. Lee, L. Wang, S. Sorgenfrei, K. Watanabe, T. Taniguchi, P. Kim, K. L. Shepard, and J. Hone, Nat. Nanotechnol. **5**, 722 (2010).

[4] A. Splendiani, L. Sun, Y. Zhang, T. Li, J. Kim, C.-Y. Chim, G. Galli, and F. Wang, Nano Lett. **10**, 1271 (2010); K. F. Mak, C. Lee, J. Hone, J. Shan, and T. F. Heinz, Phys. Rev. Lett. **105**, 136805 (2010).

[5] M. Kuwabara, D. R. Clarke, and D. A. Smith, Appl. Phys. Lett. **56**, 2396 (1990).

[6] W. Pong and C. Durkan, J. Phys.: Appl. Phys. **38**, R329 (2005).

[7] I. Amidror, *The Theory of the Moiré Phenomenon*, Vol. 1 (Springer, London, 2009).

[8] G. Li, A. Luican, J. M. B. Lopes dos Santos, A. H. Castro Neto, A. Reina, J. Kong, and E. Y. Andrei, Nat. Phys. **6**, 109 (2010); A. Luican, G. Li, A. Reina, J. Kong, R. R. Nair, K. S. Novoselov, A. K. Geim, and E. Y. Andrei, Phys. Rev. Lett. **106**, 126802 (2011); T. Ohta, J. T. Robinson, P. J. Feibelman, A. Bostwick, E. Rotenberg, and T. E. Beechem, *ibid.* **109**, 186807 (2012).

[9] M. Yankowitz, J. Xue, D. Cormode, J. D. Sanchez-Yamagishi, K. Watanabe, T. Taniguchi, P. Jarillo-Herrero, P. Jacquod, and B. J. LeRoy, Nat. Phys. **8**, 382 (2012).

[10] P. G. Harper, Proc. Phys. Soc. London **68**, 874 (1955); D. R. Hofstadter, Phys. Rev. B **14**, 2239 (1976).

[11] C. Albrecht, J. H. Smet, K. von Klitzing, D. Weiss, V. Umansky, and H. Schweizer, Phys. Rev. Lett. **86**, 147 (2001).

[12] C. R. Dean, L. Wang, P. Maher, C. Forsythe, F. Ghahari, Y. Gao, J. Katoch, M. Ishigami, P. Moon, M. Koshino, T. Taniguchi, K. Watanabe, K. L. Shepard, J. Hone, and P. Kim, Nature (London) **497**, 598 (2013); B. Hunt, J. D. Sanchez-Yamagishi, A. F. Young, M. Yankowitz, B. J. LeRoy, K. Watanabe, T. Taniguchi, P. Moon, M. Koshino, P. Jarillo-Herrero, and R. C. Ashoori, Science **340**, 1427 (2013); L. A. Ponomarenko, R. V. Gorbachev, G. L. Yu, D. C. Elias, R. Jalil, A. A. Patel, A. Mishchenko, A. S. Mayorov, C. R. Woods, J. R. Wallbank, M. Mucha-Kruczynski, B. A. Piot, M. Potemski, I. V. Grigorieva, K. S. Novoselov, F. Guinea, V. I. Fal'ko, and A. K. Geim, Nature (London) **497**, 594 (2013).

[13] R. Bistritzer and A. H. MacDonald, Phys. Rev. B **84**, 035440 (2011); M. Kindermann and E. J. Mele, *ibid.* **84**, 161406 (2011); M.-Y. Choi, Y.-H. Hyun, and Y. Kim, *ibid.* **84**, 195437 (2011); P. Moon and M. Koshino, *ibid.* **85**, 195458 (2012); Y. Hasegawa and M. Kohmoto, *ibid.* **88**, 125426 (2013); X. Chen, J. R. Wallbank, A. A. Patel, M. Mucha-Kruczyński, E. McCann, and V. I. Fal'ko, *ibid.* **89**, 075401 (2014).

[14] Z. F. Wang, F. Liu, and M. Y. Chou, Nano Lett. **12**, 3833 (2012).

[15] J. M. B. Lopes dos Santos, N. M. R. Peres, and A. H. Castro Neto, Phys. Rev. Lett. **99**, 256802 (2007).

[16] G. Trambly de Laissardiere, D. Mayou, and L. Magaud, Nano Lett. **10**, 804 (2010).

[17] E. J. Mele, Phys. Rev. B **81**, 161405 (2010); **84**, 235439 (2011); J. Phys. D **45**, 154004 (2012).

[18] M. Kindermann and P. N. First, Phys. Rev. B **83**, 045425 (2011); M. Kindermann, B. Uchoa, and D. L. Miller, *ibid.* **86**, 115415 (2012).

[19] R. Bistritzer and A. H. MacDonald, Phys. Rev. B **81**, 245412 (2010).
[20] S. Shallcross, S. Sharma, E. Kandelaki, and O. A. Pankratov, Phys. Rev. B **81**, 165105 (2010); S. Shallcross, S. Sharma, and O. A. Pankratov, Phys. Rev. Lett. **101**, 056803 (2008); W. Landgraf, S. Shallcross, K. Türschmann, D. Weckbecker, and O. A. Pankratov, Phys. Rev. B **87**, 075433 (2013); S. Shallcross, S. Sharma, and O. A. Pankratov, *ibid.* **87**, 245403 (2013).
[21] Z. D. Chu, W.-Y. He, and L. He, Phys. Rev. B **87**, 155419 (2013).
[22] R. Bistritzer and A. H. MacDonald, Proc. Natl. Acad. Sci. USA **108**, 12233 (2011).
[23] J. M. B. Lopes dos Santos, N. M. R. Peres, A. H. Castro Neto, Phys. Rev. B **86**, 155449 (2012).
[24] R. de Gail, M. O. Goerbig, F. Guinea, G. Montambaux, A. H. Castro Neto, Phys. Rev. B **84**, 045436 (2011).
[25] P. San-Jose, J. González, and F. Guinea, Phys. Rev. Lett. **108**, 216802 (2012).
[26] P. San-Jose and E. Prada, Phys. Rev. B **88**, 121408(R) (2013).
[27] T. Stauber, P. San-Jose, and L. Brey, New J. Phys. **15**, 113050 (2013).
[28] J. Gonzalez, Phys. Rev. B **88**, 125434 (2013).
[29] C. J. Tabert and E. J. Nicol, Phys. Rev. B **87**, 121402(R) (2013).
[30] P. Moon and M. Koshino, Phys. Rev. B **87**, 205404 (2013).
[31] G. Giovannetti, P. A. Khomyakov, G. Brocks, P. J. Kelly, and J. van den Brink, Phys. Rev. B **76**, 073103 (2007).
[32] B. Sachs, T. O. Wehling, M. I. Katsnelson, and A. I. Lichtenstein, Phys. Rev. B **84**, 195414 (2011).
[33] J. Slawinska, I. Zasada, and Z. Klusek, Phys. Rev. B **81**, 155433 (2010).
[34] M. Bokdam, P. A. Khomyakov, G. Brocks, Z. Zhong, and P. J. Kelly, Nano Lett. **11**, 4631 (2011).
[35] Arnaud Raoux, *Moiré effects in Bilayers Systems* (Stage Long De Recherche Report, École Normale Supérieure, 2011).
[36] J. R. Wallbank, A. A. Patel, M. Mucha-Kruczynski, A. K. Geim, and V. I. Fal'ko, Phys. Rev. B **87**, 245408 (2013).
[37] M. Mucha-Kruczynski, J. R. Wallbank, and V. I. Fal'ko, Phys. Rev. B **88**, 205418 (2013).
[38] C. Ortix, L. Yang, and J. van den Brink, Phys. Rev. B **86**, 081405(R) (2012).
[39] P. Giannozzi, S. Baroni, N. Bonini, M. Calandra, R. Car, C. Cavazzoni, D. Ceresoli, G. L. Chiarotti, M. Cococcioni, I. Dabo, A. Dal Corso, S. Fabris, G. Fratesi, S. de Gironcoli, R. Gebauer, U. Gerstmann, C. Gougoussis, A. Kokalj, M. Lazzeri, L. Martin-Samos, N. Marzari, F. Mauri, R. Mazzarello, S. Paolini, A. Pasquarello, L. Paulatto, C. Sbraccia, S. Scandolo, G. Sclauzero, A. P. Seitsonen, A. Smogunov, P. Umari, and R. M. Wentzcovitch, J. Phys.: Condens. Matter **21**, 395502 (2009).
[40] A. A. Mostofi, J. R. Yates, Y.-S. Lee, I. Souza, D. Vanderbilt, and N. Marzari, Comp. Phys. Commun. **178**, 685 (2008).
[41] N. Marzari, A. A. Mostofi, J. R. Yates, I. Souza, and D. Vanderbilt, Rev. Mod. Phys. **84**, 1419 (2012).
[42] J. Jung and A. H. MacDonald, Phys. Rev. B **87**, 195450 (2013).
[43] J. Jung and A. H. MacDonald, arXiv:1309.5429.
[44] C.-H. Park, L. Yang, Y.-W. Son, M. L. Cohen, and S. G. Louie, Nat. Phys. **4**, 213 (2008); Phys. Rev. Lett. **101**, 126804 (2008); L. Brey and H. A. Fertig, *ibid.* **103**, 046809 (2009); M. Barbier, F. M. Peeters, P. Vasilopoulos, and J. M. Pereira, Phys. Rev. B **77**, 115446 (2008).
[45] M. A. H. Vozmediano, M. I. Katsnelson, and F. Guinea, Phys. Rep. **496**, 109 (2010).
[46] J. Gonzalez, F. Guinea, and M. A. H. Vozmediano, Nucl. Phys. B **424**, 595 (1994); Y. Barlas, T. Pereg-Barnea, M. Polini, R. Asgari, and A. H. MacDonald, Phys. Rev. Lett. **98**, 236601 (2007); J. Jung and A. H. MacDonald, Phys. Rev. B **84**, 085446 (2011).
[47] J. C. W. Song, A. V. Shytov, and L. S. Levitov, Phys. Rev. Lett. **111**, 266801 (2013).
[48] J. Jung, P. García-González, J. F. Dobson, R. W. Godby, Phys. Rev. B **70**, 205107 (2004).
[49] A. Marini, P. García-González, and A. Rubio, Phys. Rev. Lett. **96**, 136404 (2006).
[50] S. Lebegue, J. Harl, Tim Gould, J. G. Angyan, G. Kresse, and J. F. Dobson, Phys. Rev. Lett. **105**, 196401 (2010).
[51] T. Björkman, A. Gulans, A. V. Krasheninnikov, and R. M. Nieminen, Phys. Rev. Lett. **108**, 235502 (2012).